

SOLVING ATOMIC STRUCTURES USING STATISTICAL MECHANICAL SEARCHES ON
X-RAY SCATTERING DERIVED POTENTIAL ENERGY SURFACES

by

Christopher James Wright

Bachelor of Science
Brown University 2014

Submitted in Partial Fulfillment of the Requirements

for the Degree of Masters of Science in

Chemical Engineering

College of Engineering and Computing

University of South Carolina

2016

Accepted by:

Xiao-Dong Zhou, Major Professor

Mark Uline, Committee Member

Jochen Lauterbach, Committee Member

Thomas Vogt, Committee Member

Lacy Ford, Vice Provost and Dean of Graduate Studies

© Copyright by Christopher James Wright, 2016
All Rights Reserved.

DEDICATION

For Diane & Donald Wright

My first scientific/life advisors

ACKNOWLEDGMENTS

ABSTRACT

Engineering the next generation of materials, especially nanomaterials, requires a detailed understanding of the material's underlying atomic structure. Understanding these structures we can obtain a better understanding of the structure-property relationship, allowing for a property driven rational design of the material structure on the atomic level. Even more importantly, understanding the structure in-situ will allow the reversal of the flow of information, translating stimuli and responses on the macroscopic system level to changes in the atomic structure. Despite the importance of atomic structures for designing materials, solving the atomic structure of materials is difficult both experimentally and computationally. Atomic pair distribution functions (PDFs) have been shown to provide information on atomic structure, although extracting the PDF from x-ray total scattering measurements can be difficult. Computationally, translating the PDF to an atomic structure requires the search of a very high dimensional space and can be computationally expensive.

This work aims to address these issues by developing 1) novel statistical mechanical approaches to solving material structures, 2) fast simulation of x-ray total scattering and atomic pair distribution functions (PDFs), and 3) data processing procedures for experimental x-ray total scattering measurements. First, experimentally derived potential energy surfaces (PES) and the statistical mechanical ensembles used to search them are developed. Then the mathematical and computational framework for the PDF and its gradients will be discussed. The combined PDF-PES-ensemble system will be benchmarked against a series of nanoparticle structures to ascertain the efficiency and effectiveness of the system. Experimental data processing proce-

dures, which maximize the usable data, will be presented. Finally, preliminary results from experimental x-ray total scattering measurements will be discussed. This work presents one of the most complete end-to-end systems for processing and modeling x-ray total scattering PDF data, potentially allowing for high-throughput structural solution.

TABLE OF CONTENTS

DEDICATION	iii
ACKNOWLEDGMENTS	iv
ABSTRACT	v
LIST OF TABLES	xii
LIST OF FIGURES	xii
TODO LIST	1
CHAPTER 1 STATISTICAL MECHANICAL ENSEMBLES AND POTENTIAL ENERGY SURFACES	5
1.1 Introduction	5
1.2 Potential Energy Surfaces	5
Experimentally Derived Potential Energy Surfaces	6
Potentials	6
Forces	7
1.3 Ensembles	8
Monte Carlo Modeling	9
Hamiltonian Monte Carlo	9
No-U-Turn-Sampling	10
Grand Canonical Ensemble	11
Ensemble description	11
Grand Canonical Monte Carlo	11
GCMC biasing	12

CHAPTER 2 ATOMIC PAIR DISTRIBUTION FUNCTION: THEORY AND COMPUTATION	14
2.1 Theory	14
Derivation	14
Analytical Gradients	14
Without ADPs	16
Periodic Boundary Conditions	16
2.2 Computation	17
HPC and GPUs	17
GPUs and Parallelization	17
Map from ij space to k space	18
GPU Memory Allocation	19
CHAPTER 3 BENCHMARKING	22
3.1 PDF	22
Model Parameters	24
Au55: surface relaxed	25
Run Parameters	25
Au55: surface disordered	27
Au55: amorphous	28
Au102: triple phase	29
Starting from fcc structure	29
Marks decahedron	30
Au147	31
3.2 PDF with ADPs	31
ADP 50	31
CHAPTER 4 X-RAY TOTAL SCATTERING DATA ACQUISITION AND PRO- CESSING	37
4.1 Introduction	37
4.2 Detector Q resolution	37
4.3 Automated Mask Generation	39
Introduction	39
Algorithm Design	41
Test Cases	41

Results and Discussion	42
Conclusions	48
4.4 Automated Image Azimuthal Integration	49
4.5 Conclusions	51
 CHAPTER 5 ANNEALING AND AGGREGATION OF 2NM AU NANOPARTICLES	54
5.1 Experiments	54
NP Synthesis	54
X-ray Total Scattering Measurements	54
5.2 Data Processing	54
5.3 Data Analysis	54
5.4 Simulation	54
5.5 Structural Analysis	54
5.6 Conclusions	54
 CHAPTER 6 PHASE CHANGES AND ANNEALING DYNAMICS OF Pr_2NiO_4 AND ITS DERIVATIVES	55
6.1 Experiments	55
Pr_2NiO_4 Synthesis	55
X-ray Measurements	55
6.2 Data Processing	55
6.3 Data Analysis	55
Intra Sample Comparison	55
Inter Sample Comparison	61
6.4 Simulation	74
6.5 Conclusions	74
 CHAPTER 7 CONCLUSION	76

BIBLIOGRAPHY	77
------------------------	----

LIST OF TABLES

LIST OF FIGURES

Figure 2.1 Comparison of the CPU and GPU chip architectures	18
Figure 3.1 Au ₅₅ PDF fitting of DFT-optimized <i>c</i> -Au ₅₅ . (a) the final structural solution ($R_w=0.3\%$) with bond lengths color-coded by step of 0.05Å, (b) the target PDF(blue dots) overlaid with the PDF of the final structure (solid red lines) with the difference in green lines offset below, ?? the radial bond distribution, and (d) bond angle distribution.	26
Figure 3.2 Au ₅₅ PDF fitting of surface-disordered Au ₅₅ . a) the target structure, b) the final structural solution ($R_w=0.6\%$), c) the comparison of PDFs, d) the CN distribution with the number of atoms in either the core or the surface, e) the radial bond distribution, and f) the bond angle distribution.	32
Figure 3.3 Similar to figure 3.2 for DFT-optimized amorphous Au ₅₅	33
Figure 3.4 Similar to figure 3.2 for Au ₁₀₂ as in DFT-optimized Au ₁₀₂ MBA ₄₄ cluster.	34
Figure 3.5 Similar to Fig. 3.6 with Marks decahedron as the starting structure.	35
Figure 3.6	36
Figure 4.1 Scattering onto a flat detector	38
Figure 4.2 Q resolution as a function of Q	39
Figure 4.3 Number of pixels as a function of Q , binned at the Q resolution of the detector.	40
Figure 4.4 Generated dead/hot pixel masks for a detector with 100 bad pixels.	42
Figure 4.5 Generated dead/hot pixel masks for a detector with 300 bad pixels.	43
Figure 4.6 Generated dead/hot pixel masks for a detector with 500 bad pixels.	43

Figure 4.7 Generated dead/hot pixel masks for a detector with 1000 bad pixels.	44
Figure 4.8 Generated beamstop holder masks for a beamstop holder with 10% transmittance.	44
Figure 4.9 Generated beamstop holder masks for a beamstop holder with 30% transmittance.	45
Figure 4.10 Generated beamstop holder masks for a beamstop holder with 50% transmittance.	45
Figure 4.11 Generated beamstop holder masks for a beamstop holder with 90% transmittance.	45
Figure 4.12 Generated beamstop holder masks which is rotated away from verticle	46
Figure 4.13 Masked experimental data.	46
Figure 4.14 Masked experimental data with Pt single crystal signal.	47
Figure 4.15 Masked experimental data with Pt single crystal signal using figure's 4.13 as a starting mask.	47
Figure 4.16 Masking, average, and standard deviation of an example x-ray total scattering measurement. This image was produced with no mask. a) the image, b) the mask, c) the mean and median values, d) the standard deviation (normalized to the median), e) a closeup of the 28 \AA^{-1} to $31 \text{ \AA}^{-1}Q$ range for the mean and median, f) 28 \AA^{-1} to $31 \text{ \AA}^{-1}Q$ range for the standard deviation	50
Figure 4.17 Masking, average, and standard deviation of an example x-ray total scattering measurement. This image was produced with only an edge mask. a) the image, b) the mask, c) the mean and median values, d) the standard deviation (normalized to the median), e) a closeup of the 28 \AA^{-1} to $31 \text{ \AA}^{-1}Q$ range for the mean and median, f) 28 \AA^{-1} to $31 \text{ \AA}^{-1}Q$ range for the standard deviation	51

Figure 4.18 Masking, average, and standard deviation of an example x-ray total scattering measurement. This image was produced combining an edge mask and the automatically generated mask. a) the image, b) the mask, c) the mean and median values, d) the standard deviation (normalized to the median), e) a closeup of the 28 \AA^{-1} to 31 \AA^{-1} Q range for the mean and median, f) 28 \AA^{-1} to 31 \AA^{-1} Q range for the standard deviation 52

1

Fix the figures so that they don't give the full caption

TODO LIST

3	Fix the figures so that they don't give the full caption	1
4	Why is atomistic engineering important	3
5	Barriers to atomistic engineering	3
6	How are we going to attack this problem	3
7	Need to discuss Monte Carlo more, including Reverse Monte Carlo	9
8	Need to put HMC into the Stat Mech Formalism, it is kinda canonical, 9 except that it has a random momenta which is specified and not temperature.	9
10	Need the official criteria for HMC	10
11	Talk about the advances NUTS gives us	10
12	What limitations in RMC/HMC/NUTS/Cannonical ensembles in general 13 force us to move to GCMC	11
14	Include figure which shows the configurational biasing map	13
15	Need to include PBC ADP math	16
16	Also should include PBC gradients, although they are trivial, maybe?	17
17	Include Speed Benchmarks Here	21
18	This entire section needs some rewritting to distinguish this from the paper .	22
19	Put this somewhere	26
20	masking parameters	55
21	integration parameters	55
22	PDF parameters	55

23

INTRODUCTION

24

Why is atomistic engineering important

25 Engineering materials and chemicals on the atomic scale has been a goal for the
26 chemistry, physics, materials science, and chemical engineering fields long before the
27 advent of nanomaterials. Realizing this goal could lead to durable fuel cell catalysts,
28 more bioavailable pharmaceuticals, and radiation damage resistant spacecraft shielding.

29

Barriers to atomistic engineering

30 Before we can even think of making atomistically exact structures, durable struc-
31 tures, or structures which change in reproducible ways, we need to know the atomic
32 structure exactly.

33

How are we going to attack this problem

34 This work addresses these issues by developing a methodology for solving the
35 structure of nanomaterials by matching experimental x-ray scattering data with sim-
36 ulated atomic structures.

37 Chapter 1 develops the statistical mechanical system used to match the theoretical
38 structure. §1.2 focuses on the development of potential energy surfaces, including
39 potential energy and force equations, which have minima where experimental results
40 and simulated structures agree the most. §1.3 will discuss statistical mechanical
41 ensembles which are used to search for minima on the potential energy surface.

42 Chapter 2 will discuss the mathematical and computational development of the
43 atomic pair distribution function (PDF). §2.2 will focus on the rapid graphical pro-
44 cessing unit based calculation of the PDF and its gradients.

45 Chapter 3 will discuss the benchmarking of the the combined statistical mechan-

46 ical optimizer and PDF calculation systems against a series of theoretical nanoparti-
47 cles, focusing on understanding limitations of the method and structure reproduction.

48 Chapter 4 will focus on the aquesition of experimental data, its management, and
49 processing. §4.2, 4.3, and 4.4 will discuss the derivation of the Q resolution function,
50 the automated masking of 2D area detectors for x-ray total scattering measurements
51 using the previously derrived Q resolution, and the impact of different averaging
52 methods and masks on azimuthal integration, respecitvly.

53

CHAPTER 1

54

STATISTICAL MECHANICAL ENSEMBLES AND POTENTIAL ENERGY SURFACES

56 1.1 INTRODUCTION

57 The approach taken in this work for solving the atomic structures of materials is one
58 of optimization. The plan is to develop a potential energy surface (PES) which has
59 minima associated with atomic structures who's properties match the experimentally
60 observed properties. Thus, the various positional variables of the structure can be
61 solved by optimizing the structure against the PES. This approach is popular in the
62 PDF community for solving the structure of materials using both extensive large box
63 models and simpler small box models.

64 In this chapter we discuss the development of the various PESs used in the PDF
65 community for comparing theoretical and experimental PDFs. Special attention will
66 be paid to the gradients of the potential energy functions, as these are important
67 to some optimization techniques. Additionally, we also discuss the use of statistical
68 mechanical ensembles for finding minima on the PES.

69 1.2 POTENTIAL ENERGY SURFACES

70 A PES simply describes the potential energy of the system as a function of all its
71 relevant coordinates in phase space, essentially providing a mapping $\mathbb{R}^n \rightarrow \mathbb{R}$. Usually
72 these coordinates are the positions of the atoms q and their conjugate the momenta p .
73 Note that there could be more variables associated with the system, for instance the

74 magnetic moments of the atoms could play a role in describing the system. In this
 75 magnetic system there would be positional variables for the atomwise spin vectors
 76 and their "momenta". Application of the term "momenta" might seem odd here, as
 77 the magnetic spin does not have a mass or a velocity. However, since the magnetic
 78 "position" is defined on the PES we need to describe its conjugate variable to properly
 79 formulate Hamiltonian dynamics and the kinetic portion of the PES.

80 **Experimentally Derived Potential Energy Surfaces**

81 Generally PESs are obtained from purely computational experiments including: ab-
 82 initio DFT, classical approximations via the embedded atom method, or even param-
 83 eter driven models with experimentally fitted parameters. However, one can derive
 84 a PES from an experiment which describes how well the model reproduces the ex-
 85 perimental data. In this case one needs a theoretical and computational framework
 86 mapping the atomistic variables of the simulation to the same space of the data ob-
 87 tained from the experiment. This allows the experiment to be compared directly
 88 against the predicted data via an experimentally derived PES.

89 **Potentials**

90 For an experiment which produces 1D data, like powder diffraction, EXAFS or XPS,
 91 the implemented potentials are:

$$\chi^2 = \sum_{a=a_{\min}}^{a_{\max}} (A_{\text{obs}} - \alpha A_{\text{calc}})^2 \quad (1.1)$$

$$Rw = \sqrt{\frac{\sum_{a=a_{\min}}^{a_{\max}} (A_{\text{obs}} - \alpha A_{\text{calc}})^2}{\sum_{a=a_{\min}}^{a_{\max}} A_{\text{obs}}^2}} \quad (1.2)$$

$$\chi^2_{\text{INVERT}} = \frac{1}{N} \sum_j \sum_r [A_{\text{obs}}(r) - \alpha A_{j,\text{calc}}(r)]^2 \quad (1.3)$$

$$\alpha = \frac{\sum_{a=a_{\min}}^{a_{\max}} A_{\text{obs}} A_{\text{calc}}}{\sum_{a=a_{\min}}^{a_{\max}} A_{\text{calc}}^2} = \frac{\vec{A}_{\text{obs}} \cdot \vec{A}_{\text{calc}}}{|\vec{A}_{\text{calc}}|^2} \quad (1.4)$$

95 where A_{calc} and A_{obs} are the calculated and observed 1D experimental data and $A_{calc,j}$
 96 is the calculated data for a single atom interacting with the other atoms of the system.
 97 Note that A_{calc} has a dependence on q , the positions of the system.

98 The Rw and χ^2 potentials have been reported numerous times. [?] However, the
 99 INVERT potential is fairly new and aims to incorporate descriptions of the structural
 100 symmetry into the PES. [2, 3] In the case of the INVERT potential NMR or other
 101 symmetry sensitive data is used to describe the number of unique atomic coordina-
 102 tions. This is then used to describe the number of unique atomwise pair distribution
 103 functions, thus causing systems with more or less unique coordination environments
 104 to be higher in energy. This approach has been shown to be useful for C_{60} and other
 105 systems which are highly symmetric, creating a PES with an easier to find minima.
 106 [2, 3] However, many times this kind of data is unavailable when refining the struc-
 107 ture causing the potential to be less useful. Additionally, this potential introduces
 108 an element of user bias as the refiner must decide, based on some spectroscopic data,
 109 how many unique environments are in the material. This bias could be removed by
 110 using one of the other potentials with a method for simulating the observed spectra,
 111 allowing the computational system decide what structures properly reproduce all the
 112 observed data.

113 Forces

$$\vec{\nabla}\chi^2 = -2 \sum_{a=a_{\min}}^{a_{\max}} (\alpha \frac{\partial A_{calc}}{\partial \gamma_{i,w}} + A_{calc} \frac{\partial \alpha}{\partial \gamma_{i,w}})(A_{obs} - \alpha A_{calc}) \quad (1.5)$$

$$\vec{\nabla}Rw = \frac{Rw}{\chi^2} \sum_{a=a_{\min}}^{a_{\max}} (\alpha \frac{\partial A_{calc}}{\partial \gamma_{i,w}} + A_{calc} \frac{\partial \alpha}{\partial \gamma_{i,w}})(\alpha A_{calc} - (A_{obs})) \quad (1.6)$$

$$\vec{\nabla}\chi_{INVERT}^2 = \frac{-2}{N} \sum_{a=a_{\min}}^{a_{\max}} \sum_j (\alpha \frac{\partial A_{j,calc}}{\partial \gamma_{i,w}} + A_{j,calc} \frac{\partial \alpha}{\partial \gamma_{i,w}})(A_{obs} - \alpha A_{j,calc}) \quad (1.7)$$

$$\frac{\partial \alpha}{\partial \gamma_{i,w}} = \frac{(\sum_{a=a_{\min}}^{a_{\max}} A_{obs} \frac{\partial A_{calc}}{\partial \gamma_{i,w}} - 2\alpha \sum_{a=a_{\min}}^{a_{\max}} A_{calc} \frac{\partial A_{calc}}{\partial \gamma_{i,w}})}{\sum_{a=a_{\min}}^{a_{\max}} A_{calc}^2} \quad (1.8)$$

117 where $\gamma_{i,w}$ is the i th arbitrary positional variable in the w th direction. The concept
118 of an "arbitrary positional variable" might seem a bit cumbersome but it allows us
119 to define the forces for any atomic parameter which can be represented as a vector
120 in 3-space. This comes in handy when trying to define the forces acting on variables
121 like anisotropic displacement parameters or atomic magnetic spins.

122 ALSO COMPARE RW AND CHI**2, POTENTIALY WITH A FIGURE.

123 1.3 ENSEMBLES

124 While PESs describe which atomic configurations are the most desirable and how
125 the atoms would like to get there, the ensemble describes how the atoms move on
126 the PES. The abstraction of the PES from the ensemble is an important one, as it
127 allows for the reuse and exchange of both PESs and ensembles for a wide array of
128 problems. Statistical mechanical ensembles can be described in two ways, analytically
129 and stochastically. For long simulation times and fine enough numerical or analytical
130 integration these two descriptions should be identical.

131 In either case one starts by defining the Hamiltonian, \mathcal{H} , as the total energy of
132 the system. Thus, the Hamiltonian is described as the sum of the potential $U(q)$ and
133 kinetic $K(p)$ energies, where q is the positions of the atoms and p is their momenta

$$\mathcal{H}(q, p) = U(q) + K(p) \quad (1.9)$$

134 where $K(p) = \frac{1}{2} \sum_i \frac{p_i^2}{m_i}$ and i denotes the i th particle.

135 Analytically one generally defines a partition function, which describes the sum of
136 probabilities over all potential atomic states.

$$\Xi = \sum_i P_i(q, p)$$

137 where P_i is the probability of the i th state and is a function of the total energy of
138 that state. This partition function can then be used to obtain the probability of any

139 specific state. The relationship of the probability of a state to the state's energy
140 and other properties depends on the ensemble being used. For the microcanonical
141 ensemble the probability of a state is:

$$P(q, p) = \frac{\delta(\mathcal{H}(q, p) - E)}{W} \quad (1.10)$$

142 where E is the energy of the system, W is the total number of states in the system,
143 and δ is the Dirac Delta Function.

144 However, for the canonical ensemble the probability is:

$$P(q, p) = \exp\left(\frac{E - \mathcal{H}(q, p)}{k_b T}\right) \quad (1.11)$$

145 Monte Carlo Modeling

146 Monte Carlo can be used to simulate a statistical mechanical ensemble which can
147 not be solved analytically. In most Monte Carlo systems the ensemble is simulated by
148 randomly changing one of the system parameters and comparing the energy of the
149 new system against the energy of the old system. If the energy of the new system is
150 lower than the current energy then the new configuration is accepted. Otherwise the
151 new system is rejected unless

$$\exp\left(\frac{-\Delta E}{E_T}\right) < u$$

152 where u is a random number $[0, 1]$ and E_T is the thermal energy characteristic to the
153 system.

154 Need to discuss Monte Carlo more, including Reverse Monte Carlo

155 Hamiltonian Monte Carlo

156 Need to put HMC into the Stat Mech Formalism, it is kinda canonical, except
that it has a random momenta which is specified and not temperature.

In order to model dynamics we need to describe the motion of the particles in our system, thus:

$$\frac{dq_i}{dt} = \frac{\partial \mathcal{H}}{\partial p_i} = p_i \quad (1.12)$$

$$\frac{dp_i}{dt} = -\frac{\partial \mathcal{H}}{\partial q_i} = -\vec{\nabla}U \quad (1.13)$$

Using these equations we can derive the position and momentum vectors at any point in time using the leap-frog algorithm:

$$p_i(t + \delta t/2) = p_i(t) - \frac{\delta t}{2} \frac{\partial}{\partial q_i} U(q(t)) \quad (1.14)$$

$$q_i(t + \delta t) = q_i(t) + \delta t * p_i(t + \delta t/2) \quad (1.15)$$

$$p_i(t + \delta t) = p_i(t + \delta t/2) - \frac{\delta t}{2} \frac{\partial}{\partial q_i} U(q(t + \delta t)) \quad (1.16)$$

157 Note that $\frac{\partial}{\partial q_i}$ is the gradient with respect to q where i denotes the i th atom being
158 moved. Using this notation the gradient is

$$\vec{\nabla}U = \begin{bmatrix} \frac{\partial U}{\partial q_{0,x}} & \frac{\partial U}{\partial q_{0,y}} & \frac{\partial U}{\partial q_{0,z}} \\ \vdots & \frac{\partial U}{\partial q_{i,w}} & \vdots \\ \frac{\partial U}{\partial q_{n,x}} & \frac{\partial U}{\partial q_{n,y}} & \frac{\partial U}{\partial q_{n,z}} \end{bmatrix} = \begin{bmatrix} \vec{\mathcal{F}}_0 \\ \vdots \\ \vec{\mathcal{F}}_i \\ \vdots \\ \vec{\mathcal{F}}_n \end{bmatrix} \quad (1.17)$$

159 where $\frac{\partial}{\partial q_{i,w}}$ is the derivative with respect to q where w denotes direction of the derivative (x , y , or z), n is the number of atoms and U is the potential which depends on q , and $\vec{\mathcal{F}}_i$ is the "force" on the i th atom.

162 Need the official criteria for HMC

163 **No-U-Turn-Sampling**

164 Talk about the advances NUTS gives us

165 **Grand Canonical Ensemble**

What limitations in RMC/HMC/NUTS/Cannonical ensembles in general force us
166 to move to GCMC

167 **Ensemble description**

168 In the Grand Canonical Ensemble (GCE) two sets of variables are allowed to change,
169 the atomic positions and the total number of atoms and their associated identities.
170 These two variables are controlled by temperature and chemical potential. The par-
171 tition function is

$$\Xi = e^{-\beta(\mathcal{H}+\mu)} \quad (1.18)$$

172 This is translated into a Monte Carlo system, producing Grand Canonical Monte
173 Carlo (GCMC).

174 **Grand Canonical Monte Carlo**

175 While the probabilities for atomic motion are the same as in the Canonical Ensemble,
176 the addition or removal of an atom have their own probabilities. For the addition of
177 an atom the probability is formally:

$$\min[1, \frac{V}{(N+1)\Lambda(T)^3} e^{-\beta\Delta U + \beta\mu}] \quad (1.19)$$

178 Similarly the removal of an atom has the probability:

$$\min[1, \frac{(N)\Lambda(T)^3}{V} e^{-\beta\Delta U - \beta\mu}] \quad (1.20)$$

179 However, both of these equations depend of the overall simulation volume and the
180 thermal wavelength, which is undesirable as these are not really properties that we
181 are of interest to these simulations. Thus, we roll them into the definition of the
182 chemical potential, essentially setting the base chemical potential to counteract these
183 effects. This makes certain that our simulation does not change if we change the

184 overall cell volume. A GCMC move consists of creating a new atomic configuration,
185 where an atom has been added or removed, and checking the above criteria. However,
186 previous results have shown that this method is computationally expensive in dense
187 liquids, and exceedingly expensive in solid materials. The long simulation times
188 are due to the random nature of the atomic additions or removals which produce:
189 over-tightly packed atoms, atoms in the middle of nowhere, or unphysical vacancies.
190 These configurations are rejected by the GCMC criteria but their probability of being
191 sampled is much higher than configurations which are lower in energy, since the
192 number of incorrect ways to add/remove atoms is much larger than the correct ways.
193 Thus we have implemented methods for biasing the atomic addition positions and
194 the atomic removals toward configurations which are more likely to be accepted.

195 GCMC biasing

196 The first method is to remove some of the excess options from the probability pool.
197 Initially the insertion positions are calculated at random using a random number gen-
198 erator and scaled to the size of the simulation cell. This produces probabilities which
199 have floating point level precision, which is effectively infinite. While this produces
200 a potentially infinite number of ways to create energetically favorable configurations,
201 the infinite ways to produce bad configurations is much larger. Thus we can limit this
202 by moving to voxels. In this case atoms are added to the center of voxels which have
203 a pre-set resolution, limiting our total number of valid addition points. While this
204 could produce some problems with ergodicity, we avoid this by allowing the atoms to
205 translate throughout the system. Each voxel has a probability of being tried:

$$P_{i,j,k} = \frac{xyz}{abc} \quad (1.21)$$

206 where x, y, z and a, b, c are the resolutions and cell side lengths in the cardinal di-
207 rections, respectively. While this does help to limit the total probability space it
208 does not tell us which voxels are likely to lead to better configurations, leading to

209 many rejected atomic additions. To combat this issue we can weigh the individual
210 voxels, giving more probability to voxels which show promise and less to those with
211 less likelihood to be accepted.

212 The approach most likely to yield success would be to measure the change in
213 potential energy associated with the addition of an atom at the center of the voxel
214 where the probability of a voxel to be tried is:

$$P_{i,j,k} = \frac{e^{\beta\Delta U_{i,j,k}}}{\sum_{i,j,k} e^{\beta\Delta U_{i,j,k}}} \quad (1.22)$$

215 where $\Delta U_{i,j,k}$ is the change in energy. However, calculating $\Delta U_{i,j,k}$ can be particu-
216 larly expensive, especially when calculating scattering from atomic positions. The
217 computational expense can be mitigated by using a cheaper potential, if only for the
218 evaluation of the voxel energy, as previously shown. Similar to previous work we can
219 use the Lennard Jones potential to approximate the addition potential.

220 Include figure which shows the configurational biasing map

221 CHAPTER 2

222 ATOMIC PAIR DISTRIBUTION FUNCTION:
223 THEORY AND COMPUTATION

224 2.1 THEORY

225 To properly understand the PDF and its limitations we need to derive its mathemat-
226 ics. The PDF has been previously derived many times so it is not rederived here.
227 This discussion of the PDF and its gradients use the notation of Farrow and Billinge.
228 [6]

229 Derivation

230 Analytical Gradients

231 Many optimization algorithms and simulations methodologies, including HMC, re-
232 quire not only the potential energy of a given configuration but also the forces acting
233 on that configuration. These forces are described by the gradient of potential energy
234 of the system which in turn requires the gradient of the PDF. As previously shown the
235 PDF is the Fourier Transform of the Debye equation. Since the Fourier Transform is
236 expressed as an integral we can exchange the order of the gradient and the integral,
237 allowing us to calculate the analytical gradient of the Debye equation and FFT the
238 resulting function. The Debye equation, with a Debye-Waller vibrational correction
239 is

$$F(Q) = \frac{1}{N\langle f \rangle^2} \sum_{j \neq i} f_i^*(Q) f_j(Q) \exp(-\frac{1}{2}\sigma_{ij}^2 Q^2) \frac{\sin(Qr_{ij})}{r_{ij}} \quad (2.1)$$

240 where

$$\sigma_{ij}^2 = (\vec{u}_{ij} * \hat{d}_{ij})^2 \quad (2.2)$$

$$\vec{u}_{ij} = \vec{u}_i - \vec{u}_j \quad (2.3)$$

$$\hat{d}_{ij} = \frac{\vec{d}_{ij}}{r_{ij}} \quad (2.4)$$

$$r_{ij} = \|\vec{d}_{ij}\| \quad (2.5)$$

$$\vec{d}_{ij} = \begin{bmatrix} q_{ix} - q_{jx} \\ q_{iy} - q_{jy} \\ q_{iz} - q_{jz} \end{bmatrix} \quad (2.6)$$

241 where Q is the scatter vector, f_i is atomic scattering factor of the i th atom, and r_{ij}
 242 is the distance between atoms i and j and has q dependence. For simplicities sake
 243 we will break up $F(Q)$ so that

$$F(Q) = \alpha \sum_{j \neq i} \beta_{ij} \tau_{ij} \Omega_{ij} \quad (2.7)$$

244 where

$$\alpha = \frac{1}{N\langle f \rangle^2} \quad (2.8)$$

$$\beta_{ij} = f_i^*(Q) f_j(Q) \quad (2.9)$$

$$\tau_{ij} = \exp(-\frac{1}{2} \sigma_{ij}^2 Q^2) \quad (2.10)$$

$$\Omega_{ij} = \frac{\sin(Qr_{ij})}{r_{ij}} \quad (2.11)$$

245 The derivatives are as follows:

$$\frac{\partial}{\partial q_{i,w}} F(Q) = \alpha \sum_j \beta_{ij} \left(\frac{\partial \tau_{ij}}{\partial q_{i,w}} \Omega_{ij} + \tau_{ij} \frac{\partial \Omega_{ij}}{\partial q_{i,w}} \right) \quad (2.12)$$

246 where

$$\frac{\partial \Omega_{ij}}{\partial q_{i,w}} = \frac{Q \cos(Qr_{ij}) - \Omega_{ij}}{r_{ij}^2} (q_{i,w} - q_{j,w}) \quad (2.13)$$

$$\frac{\partial \tau_{ij}}{\partial q_{i,w}} = \frac{\sigma_{ij} Q^2 \tau_{ij}}{r_{ij}^3} ((q_{i,w} - q_{j,w}) \sigma_{ij} - (u_{i,w} - u_{j,w}) r_{ij}^2) \quad (2.14)$$

247 Since \vec{u}_{ij} is a variable as well, we need the derivative with respect to it as well.

248 Thus

$$\frac{\partial}{\partial u_{i,w}} F(Q) = \alpha \sum_j \beta_{ij} \frac{\partial \tau_{ij}}{\partial u_{i,w}} \Omega_{ij} \frac{\partial \tau_{ij}}{\partial u_{i,w}} = -\frac{\sigma_{ij} Q^2 \tau_{ij}}{r_{ij}} (q_{i,w} - q_{j,w}) \quad (2.15)$$

249 **Without ADPs**

250 Without ADPs the equations simplify down to

$$F(Q) = \frac{1}{N\langle f \rangle^2} \sum_{j \neq i} f_i^*(Q) f_j(Q) \frac{\sin(Qr_{ij})}{r_{ij}} \quad (2.16)$$

251 and

$$\frac{\partial}{\partial q_{i,w}} F(Q) = \alpha \sum_j \beta_{ij} \frac{\partial \Omega_{ij}}{\partial q_{i,w}} \quad (2.17)$$

252 use of these equations, when ADPs are not appropriate (like at cyrogenic tempera-
253 tures), greatly speeds up the computaiton.

254 **Periodic Boundary Conditions**

255 Periodic boundary conditions can be helpful when simulating extended solids or large

256 nanoparticles. In this case all the non-crystallinity is contained within the simulation

257 box and the box is repeated to create the longer distance peaks observed in the PDF.

258 To perform this we can break up the Debye equation into two main parts, the part

259 that describes the interatomic distances within the simulation box and those between

260 boxes. Neglecting the thermal motion portion:

$$F(Q) = \frac{1}{N\langle f \rangle^2} \left(\sum_{j \neq i} f_i^*(Q) f_j(Q) \frac{\sin(Qr_{ij})}{r_{ij}} + \sum_{i,j} f_i^*(Q) f_j(Q) \frac{\sin(QR_{ij})}{R_{ij}} \right) \quad (2.18)$$

261 where

$$R = |\vec{r} + \vec{u}| \quad (2.19)$$

$$\vec{u} = \gamma_1 * \vec{a} + \gamma_2 * \vec{b} + \gamma_3 * \vec{c} \quad (2.20)$$

262

263 Need to include PBC ADP math

264 Also should include PBC gradients, although they are trivial, maybe?

265 **2.2 COMPUTATION**

266 Simply deriving the equations for the PDF is not enough. The many body nature of
267 the PDF equation make analytical solution of the structure from the PDF impossible.
268 Thus, the PDF must be computed from a structural candidates and compared against
269 experimental results to evaluate the reliability of the model.

270 **HPC and GPUs**

271 To properly solve the structure of materials the PDF will need to be computed many
272 times and checked against experimental results. This requires computation of the
273 PDF, potentially over many atoms. Calculating these PDFs requires a fast, highly
274 parallelized, computational framework.

275 **GPUs and Parallelization**

276 Computing the PDF is an embarrassingly parallel problem. The basic procedure is
277 to calculate the reduced structure factor $F(Q)$ for each atom pair and momentum
278 transfer vector, sum over all the atom pairs, and Fourier transform the structure to
279 the PDF. The first part of this procedure is perfectly parallelizable, as each atom pair is
280 separate from the others. The summation over all the atomic reduced structure factors
281 can be parallelized via distributed summing. Lastly the FFT can be parallelized using
282 existing parallel FFT algorithms.

283 GPUs are particularly well suited to the task of computing PDFs. GPU chip
284 architecture is designed to perform many tasks simultaneously by having potentially
285 thousands of cores.

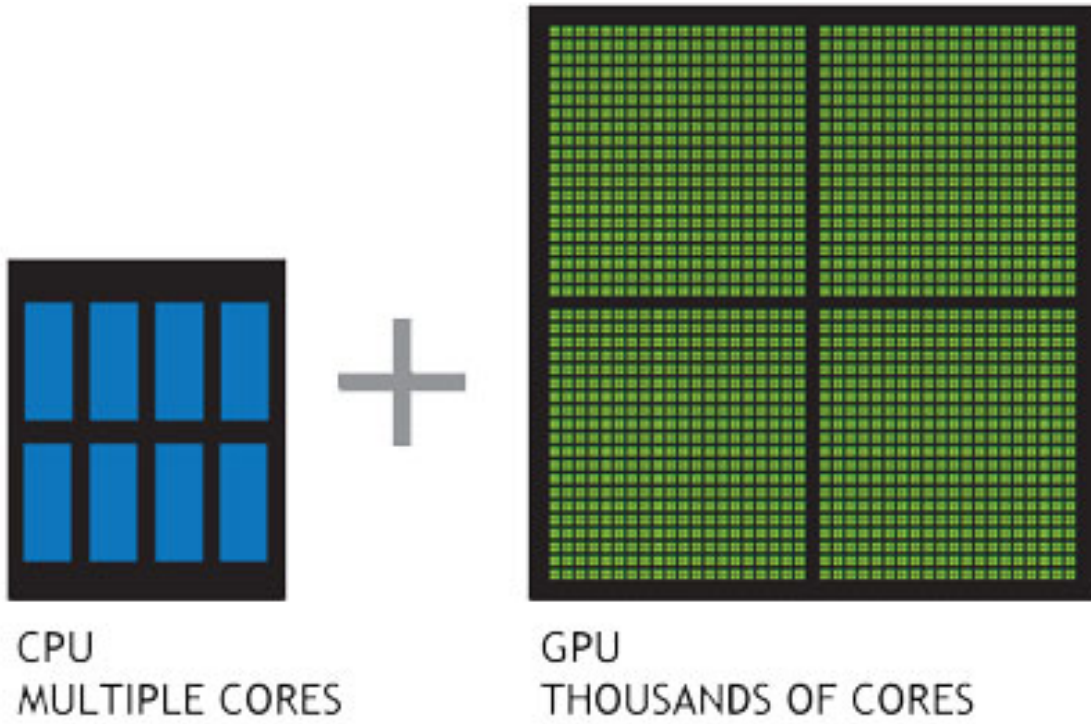


Figure 2.1: Comparison of the CPU and GPU chip architectures

286 Map from ij space to k space

287 The above equations, although formally correct, are very inefficient. $F(Q)$ and its
 288 gradient are indexed over all the atoms twice, however there are symmetries that
 289 allow us to only compute over the atom pairs essentially mapping from an $n \times n$ space,
 ij space, to a $\frac{n(n-1)}{2}$ space, k space. For $F(Q)$ we apply the following mapping where

$$\begin{array}{ccc}
 E & \xrightarrow{\psi} & E' \\
 \phi \downarrow & & \Sigma \longrightarrow Z \\
 B & \xrightarrow{\psi'} & B' \\
 & & \Sigma' \nearrow
 \end{array}$$

290

291 E denotes the atomic coordinates in ij space, E' denotes $F(Q)$ before the summation
 292 in ij space, B denotes the atomic pairs in k space, B' denotes $F(Q)$ in k space, and
 293 Z denotes the final summed $F(Q)$. For the operators, ϕ denotes the mapping from

294 ij space to k space $k = j + i * \frac{i-1}{2}$, ψ and ψ' denote the $F(Q)$ operation in ij and k
 295 space, respectivly. Σ denotes the sum over all the atoms.

296 To properly define Σ' we must establish whether $F(Q)$ is an even function. We
 297 can accomplish this by examining each of the portions of $F(Q)$, $\alpha, \beta, \tau, \Omega$. Ω is even,
 298 since r_{ij} is the interatomic distance, which is the same despite a flip of indicies, Q
 299 does not depend on the atomic indicies, and since Qr_{ij} is even so is $\sin Qr_{ij}$. Thus,
 300 Ω is even. Providing similar analysis to τ we can see that while \vec{u}_{ij} is odd, so is
 301 the unit displacement vector between the two atoms, thus the two odds cancel out.
 302 Intuitivly this makes sense, since the $F(Q)$ equation is fundamentally interested in the
 303 interatomic distances which is even. Thus, switching atom indicies does not change
 304 $F(Q)$. Due to the even nature of the $F(Q)$ operator the Σ' operator sums over all the
 305 atom pairs, and multiplies by two to reflect the double counting of the Σ operator.

For the gradient a similar mapping is used:

$$\begin{array}{ccccc} E & \xrightarrow{\psi} & E' & \xrightarrow{\Sigma} & Z \\ \phi \downarrow & & & \nearrow \tilde{\phi}\Sigma & \\ B & \xrightarrow{\psi'} & B' & & \end{array}$$

306

307 In this mapping, however, we use the $\tilde{\phi}\Sigma$ operator. This operator simultaniously
 308 performs a reverse mapping from k to ij space, and a summation with the correct
 309 symmetry. In this case the ψ and ψ' operators, which denote the $\vec{\nabla}F(Q)$ operator
 310 in ij and k space, are antisymmetric. Intuitivly this makes sense as an extension of
 311 Newton's Second Law, since each particle's interation is felt oppositely by its partner.

312 GPU Memory Allocation

313 While GPUs are very fast computational engines they tend to be memory bound.
 314 While a gradient array for a 10nm Au nanoparticle, consisting of 31,000 atoms and

315 half a billion unique distances, occupies 1.5 TB of memory a single GPU's RAM
 316 allotment varies from 4GB on a NVIDIA GTX970 to 24 GB on a NVIDIA Tesla K80.
 317 Thus, it is important to determine exactly how many atoms can fit on a GPU of
 318 arbitrary size as a function of the number of atoms and the Q range. The memory
 319 required per array is:

$$q[=]3n \quad (2.21)$$

$$d[=]3k \quad (2.22)$$

$$r[=]k \quad (2.23)$$

$$scatter[=]nQ \quad (2.24)$$

$$normalization[=]kQ \quad (2.25)$$

$$\omega[=]kQ \quad (2.26)$$

$$F_k(Q)[=]kQ \quad (2.27)$$

$$Sum[=]kQ \quad (2.28)$$

$$Sum2[=]kQ \quad (2.29)$$

$$F(Q)[=]Q \quad (2.30)$$

320 where n is the number of atoms, k is the number of unique distances, Q is the scatter
 321 vector. Each of the above arrays are used in the computation and thus must be able
 322 to be held in memory. Thus the number of atom pairs that can fit on a GPU with
 323 am bytes of available memory is:

$$k_{perGPU} = \frac{1}{16Q + 16} (-4Qn - 4Q + am - 12n) \quad (2.31)$$

324 If ADPs are included in the calculation, then the following arrays are also added to
 325 the memory allocation:

$$adps = 3n \quad (2.32)$$

$$\sigma = k \quad (2.33)$$

$$\tau = kQ \quad (2.34)$$

326 Thus the pair allotment is:

$$k_{perGPU} = \frac{-4Qn - 4Q + am - 24n}{20Q + 20} \quad (2.35)$$

327 For the Gradient we need to calculate $F(Q)$ and its gradient, so the total memory
328 overhead is equal to the previously mentioned arrays plus:

$$g_{omega} = 3kQ \quad (2.36)$$

$$g_fq = 3kQ \quad (2.37)$$

$$rtn = 3nQ \quad (2.38)$$

329 Thus the gradient allotment is:

$$\vec{\nabla}k_{perGPU} = \frac{-16Qn + am - 12n}{32Q + 16} \quad (2.39)$$

330 For the gradient with ADPs the ADP gradient array is:

$$g_tau = 3kQ \quad (2.40)$$

331 Thus the allocation is:

$$\vec{\nabla}k_{perGPU} = \frac{-16Qn + am - 24n}{48Q + 20} \quad (2.41)$$

332 These equations were solved by sympy as their validity is very important to the overall
333 reliability of the software. If the GPU is overallocated then the system may crash or
334 return meaningless results.

335 **Include Speed Benchmarks Here**

336

CHAPTER 3

337

BENCHMARKING

338

This entire section needs some rewriting to distinguish this from the paper

339

The NUTS-HMC system was tested on a series of nanoparticle (NP) benchmarks.

340

The purpose of these benchmarks is to test the ability of the NUTS-HMC system to reproduce the target PDF and its associated structure. Systems were chosen for their size, crystallinity, and interfacial differences.

343

3.1 PDF

344

The formation of NPs with both crystallographic and non-crystallographic structures [12] and with different chemical patterns [7] are well documented. For simplicity, we chose monometallic Au clusters as benchmarks and considered two groups of structures with different size and degrees of structural disorder in order to assess the reliability and efficiency of our HMC method for solving atomic structures from PDFs. The first group consists of Au_{55} clusters with different degrees of disorder, including a crystalline cluster structure in O_h (Octahedral) symmetry, a structure with a disordered surface, and an amorphous structure. The second group consists of the crystallographically solved Au_{102} structure as in the $\text{Au}_{102}\text{MBA}_{44}$ nanocrystals [8, 11]. We used optimized structures from the Density Functional Theory (DFT) as target structures and generated the corresponding PDF, G_{obs} , according to

$$G_{\text{obs}} = \frac{2}{\pi} \int_{Q_{\min}}^{Q_{\max}} Q[S_{\text{obs}}(Q) - 1] \sin(Qr) dQ \quad (3.1)$$

355 where S_{obs} is the target structure's structure factor. Since all the target structures
356 were optimized by DFT at zero Kelvin the target and model PDF profiles were
357 calculated at zero temperature, with no atomic displacement parameters (ADPs).
358 However, ADPs would have a considerable impact on the calculation of the PDF,
359 especially for nanoparticles at non-zero temperatures.

360 Spin-polarized DFT calculations were carried out using the Vienna ab initio sim-
361 ulation package (VASP) [9, 10] within the Perdew-Burke-Ernzerhof (PBE) exchange-
362 correlation functional [13]. The projected augmented wave method [1] and a kinetic
363 energy cutoff of 400 eV were used. Structural optimization was performed until the
364 total energy and ionic forces were converged to 10^{-6} eV and 10 meV/Å, respectively.
365 The amorphous Au₅₅ structures were generated by simulated annealing using the
366 classical embedded atom method potential [16]. Different annealing temperatures
367 between 1200 K and 1670 K (bulk melting temperature of Au) were used and the
368 thermally equilibrated structures were cooled down to 300 K before minimization at
369 0 K. Further optimization using DFT leads to total energies that vary within 1-2
370 eV among different amorphous structures and the lowest energy one was used as the
371 target structure. The target structure of Au₁₀₂ was taken as the Au₁₀₂ core of the
372 DFT-optimized Au₁₀₂MBA₄₄ cluster [11].

373 All systems were refined using a PES which consists of a linear combination of
374 Rw , the repulsive and attractive thresholded spring potentials. The total potential
375 energy in the Hamiltonian in Eq. (1.9) is expressed as:

$$U(q) = U_{Rw}(q) + U_{\text{spring}}(q, R_{\min}) + U_{\text{spring}}(q, R_{\max}) \quad (3.2)$$

376 The thresholded spring potentials are based on those previously proposed on by Pe-
377 terson [14], i.e. $U_{\text{spring}}(q, r_t) = \frac{\kappa}{2} \sum_{i,j} (r_{i,j} - r_t)^2$ for all atomic distance $r_{i,j}$ outside the
378 bounds of the spring threshold r_t . The resulting restoring forces on the out-of-bound
379 atoms bring the system back within the bounds of the PDF, R_{\min} and R_{\max} , and
380 therefore preventing the system from exploding or collapsing. Otherwise, incorrect

refinements may result by having atomic pair distances out of the PDF bounds. κ is the spring constant in eV/Å and the Rw potential is converted from unitless to eV via multiplication by a conversion factor λ .

Whereas the choice of the absolute values of λ and κ is somewhat arbitrary, their relative values are important in determining which term in Eq. (3.2) dominates the PES, especially when considering the effect of the simulation temperature. Generally, the ratio between the total potential energy and the temperature determines how much random motion will dominate the dynamics; a lower ratio implies that random motion will play a large role in the dynamics. The ratio between λ and κ of each spring describes how far the PDF can push the system below or above the bounds set by the spring potentials. Heuristically, too stiff a spring forbids the system to access new configurations, e.g. high energy “transition states” which may involve shorter bonds or a larger system size. Conversely, too small a spring constant makes it slower for the system to snap back within bounds and may lead to an explosion or implosion of the system, leaving the dynamics to drift aimlessly.

Model Parameters

Unless otherwise stated, the PDFs of the target and starting structures were generated using Eqn. (3.1) with a step of $\delta R = .01$ Å, $Q_{\min} = 0.1$ Å⁻¹, $Q_{\max} = 25.0$ Å⁻¹. R_{\min} and R_{\max} correspond to the first minimum before the first PDF peak and that after the last PDF peak, respectively, which ensure that the full meaningful region of the PDF is modeled. For each of the simulations, the Q resolution was calculated by

$$\delta Q = \frac{\pi}{R_{\max} + \frac{12\pi}{Q_{\max}}} \quad (3.3)$$

The HMC simulation was run with $N = 300$ iterations, a target acceptance rate of 0.65, and an average starting momentum for each NUTS iteration of 10 eVfs/Å. Both repulsive and attractive spring potentials are used with $\kappa = 200$ eV/Å and

405 thresholds matching R_{\max} and R_{\min} of the PDF, respectively. $\lambda = 300$ eV was used
406 as conversion factor for Rw . Each simulation was run with a pair of Nvidia GTX970
407 graphics cards, with one card partially occupied with desktop visualization.

408 **Au55: surface relaxed**

409 We first test our algorithm by solving the crystalline Au₅₅ (*c*-Au₅₅) cluster structure
410 from its PDF. The starting structure is taken as the bulk-cut cuboctahedron of Au₅₅
411 with a uniform bond length of 2.89 Å. Due to finite-size and surface effects, the DFT-
412 relaxed cluster structure shows a distinctively different bond length distribution as a
413 function of the bond's distance to the cluster center of mass, and therefore is difficult
414 to model with a small box approach which assumes an identical unit cell throughout
415 the whole system.

416 **Run Parameters**

417 R_{\min} and R_{\max} for this simulation were 2.45 Å and 11.4 Å, respectively, with $\delta Q =$
418 0.24 Å⁻¹. The simulation ran for approximately 34 minutes, over a total of ~40
419 thousand configurations. The results are shown in Fig. 3.1.

420 The PDF, radial bond distribution, and bond angle distribution show good agree-
421 ment between the target and final fitted structures, with a Rw of 0.3% whereas Rw
422 of the starting structure is as high as 44.8%. DFT calculations yield a total energy of
423 the final structure very close to that of the target structure (within a few meV). The
424 success in the fitting is largely attributed to the factor that the target structure is
425 only locally (and mildly) disturbed from its bulk-like counterpart and therefore there
426 is no need to overcome any high PES barriers to reach the correct solution. As shown
427 below, the situation is rather different for much more disordered target structures.
428 Interestingly, the small-box solution using PDFgui[5] yields a rather large Rw of 43%,

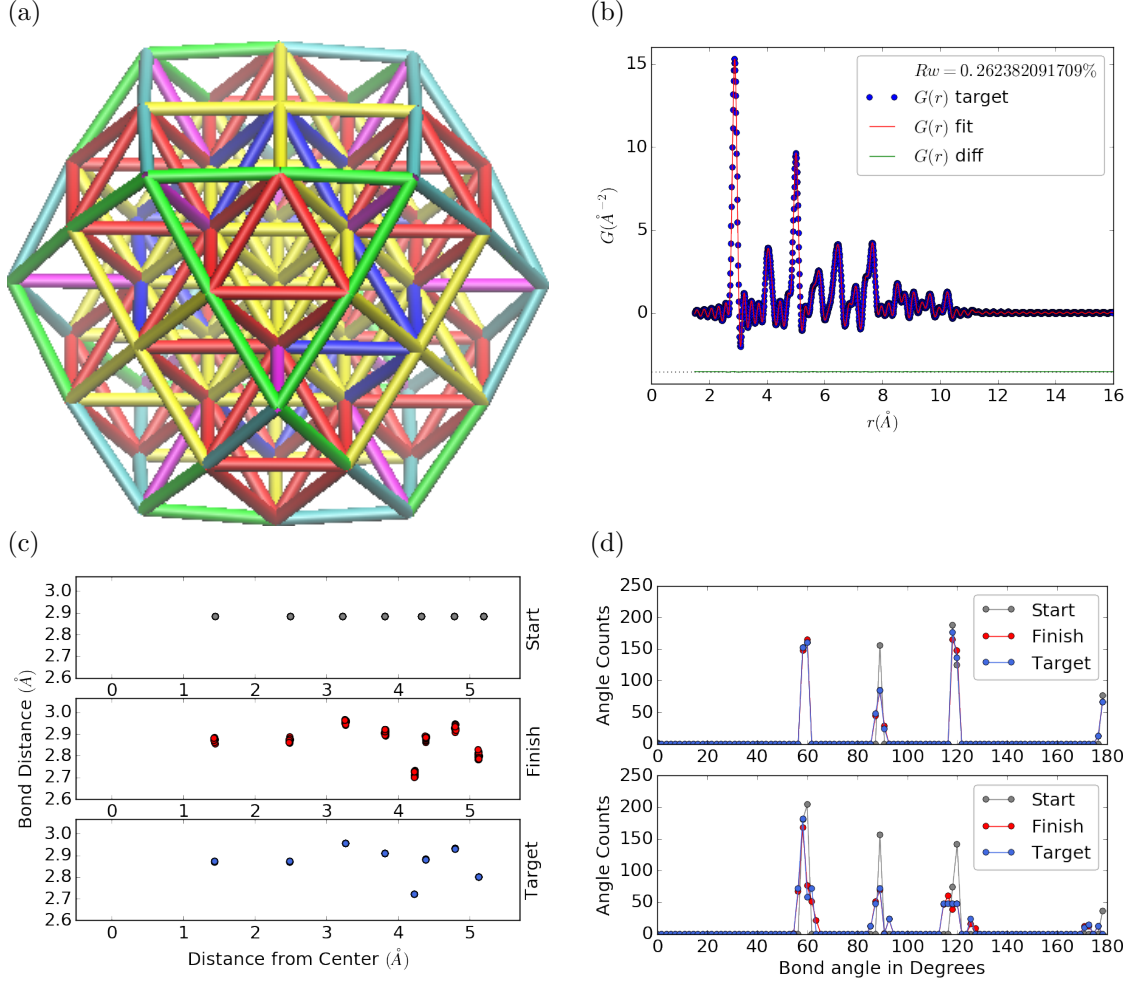


Figure 3.1: Au_{55} PDF fitting of DFT-optimized $c\text{-Au}_{55}$. (a) the final structural solution ($Rw=0.3\%$) with bond lengths color-coded by step of 0.05\AA , (b) the target PDF(blue dots) overlaid with the PDF of the final structure (solid red lines) with the difference in green lines offset below, ?? the radial bond distribution, and (d) bond angle distribution.

due to the failure to fit the surface contracted atoms with a unit cell. The PDF fits of the starting structure and small-box solution are shown

Put this somewhere

.

433 **Au55: surface disordered**

434 In addition to surface relaxation, the structure of a cluster or nanoparticle is often
435 disrupted by the presence of defects and/or ligand bound to the surface. To mimic
436 such surface disorders, we took the DFT-optimized *c*-Au₅₅ structure from case I as
437 the starting structure and randomly displaced the surface atoms with a normal distri-
438 bution of $\sigma = 0.2 \text{ \AA}$. All atoms are allowed to move in the HMC simulation, including
439 the originally undisturbed core, which is a Au₁₃ cluster with O_h symmetry.

440 R_{\min} and R_{\max} for this simulation were 1.95 Å and 12.18 Å, respectively, with
441 $\delta Q = 0.23 \text{ \AA}^{-1}$. The simulation ran for approximately 3.6 hours, over a total of ~ 270
442 thousand configurations. The results of the simulation are shown in Fig. ??.

443 Overall, good agreement is found between PDFs of the target structure and the
444 final structural solution, even out to larger r , with an $Rw = 0.6\%$ starting from an
445 $Rw = 50.4\%$ (see Fig. S2). The radial bond distribution and angle distribution
446 show reasonably good agreement, but with lower degree of crystallinity in the final
447 structure compared to the target structure. The discrepancy is most obvious in
448 the core: despite the identical core structure in the starting and target structures,
449 the core atoms were displaced in the HMC simulations in order to achieve a “best”
450 solution. This is because PDF measures the global average of interatomic distances
451 between each atomic pair and does not contain direct information about the locality
452 of such pairs, e.g. on the surface or cores. If such information is obtained a priori, for
453 example, from theoretical prediction or other experimental measurements, the core
454 structure can then be fixed and excluded from HMC dynamics.

455 Similar discrepancies are found in the CN distribution. Since the initial displace-
456 ments of the surface atoms are relatively mild, the interatomic connectivities remain
457 more or less the same and therefore the target structure has an identical CN distri-
458 bution to the starting (unperturbed) structure. This is, however, not the case for
459 the final fitted structure, which shows discernible differences, especially at the low

460 and high CN numbers. This is partly caused by the displacement of the core atoms
461 mentioned above, and partly by the lack of CN constraints for the PDF fitting, which
462 has been previously demonstrated in the case of α -Si [2]. Additional experimental
463 data, e.g. from EXAFS or NMR, may help to steer the simulations towards better
464 agreement in both PDF and CN distribution.

465 Au55: amorphous

466 Next, we turn to the case in which the entire cluster structure is disordered. We used
467 a DFT-optimized amorphous Au_{55} (a - Au_{55}) as the target structure, and the DFT-
468 relaxed c - Au_{55} cluster from Case I as the starting structure. The total energy of
469 a - Au_{55} was computed to be *lower* than that of c - Au_{55} by as large as 2.9 eV, consistent
470 with the 3.0 eV found in previous DFT work [4].

471 R_{\min} and R_{\max} for this simulation were 2.6 Å and 11.26 Å, respectively, with
472 $\delta Q = 0.25 \text{ \AA}^{-1}$. The simulation ran for approximately an hour, over a total of ~ 87
473 thousand configurations. The results of the simulation are shown in Fig. ??.

474 Our PDF fitting yielded a final structure of Rw of 1.7%, whereas that of the
475 initial structure is as high as 76.1% (see Fig. S3), due to the drastically different
476 atomic structure of the crystalline and amorphous Au_{55} clusters. Overall reasonable
477 agreement in PDF, bond angle distribution, and radial bond distance distribution
478 was found, and the wide spread of the bond lengths was qualitatively reproduced.
479 However, the mismatch in CNs is problematic, partly due to the lack of information
480 and/or constraints on the CNs. The total energy of the final structure is computed to
481 be ~ 6 eV higher than that of the target structure and the difference is substantially
482 larger than the variation among different amorphous structures computed by DFT
483 ($\Delta E_{\text{tot}} \sim \pm 1\text{-}2$ eV). Such a fitting result, despite the rather small Rw , clearly
484 indicates the importance of complementary informations and/or constraints necessary
485 for reliably solving disordered NP structures from PDF.

486 **Au102: triple phase**

487 Our final benchmark is Au₁₀₂, whose structure was initially solved by Jadzinsky and
488 co workers using x-ray crystallography [8] and further confirmed by DFT studies [11].
489 The Au₁₀₂ structure consists of three main parts, a 49-atom Marks decahedron core,
490 two C_5 caps consisting of 20 atoms each, and 13 equatorial atoms. Unlike previous
491 cases, the multi-symmetry nature of the structure, i.e. each part has its own distinct
492 symmetry, poses a challenge for PDF-based solution of the structure. This is because
493 of the atomically centralized nature of the PDF, in which each atom “sees” a density
494 of other atoms surrounding it and has a strong tendency towards becoming the center
495 of the main symmetry group. Such tendency may lead to a solution where some of
496 the correct atomic symmetries are discarded in favor of the core symmetry.

497 **Starting from fcc structure**

498 The starting structure was generated by a spherical cut of the fcc bulk lattice, with
499 two surface atoms removed to conserve the total number of Au atoms.

500 R_{\min} and R_{\max} for this simulation were 2.7 Å and 16. Å, respectively, with $\delta Q =$
501 0.18 Å⁻¹. The simulation ran for approximately two hours, over a total of ~82
502 thousand configurations. The results of the simulation are shown in Fig. 3.6.

503 The initial structure of an fcc bulk-cut cluster, had a starting Rw of 77.6% (see Fig.
504 S4), whereas the final structure has a Rw as low as 8.1%. The disagreement between
505 the final and target PDFs shows that the majority of the error is in the high R region,
506 which is related to the long range distances between the core, caps, and equatorial
507 atoms. The agreement for other structural metrics is less satisfactory. The bond
508 angle distribution for core atoms in the final structure has a poor correlation with
509 those in the target structure, with much broader peak widths. This is likely caused
510 by the high kinetic barrier to change from one high-symmetry core structure (fcc)
511 to another (Marks Decahedron). In contrast, the bond angle distribution for surface

512 atoms, which are of lower symmetry than the core, show a much better agreement.
513 This is due to the preference of Monte Carlo techniques for higher entropy, and thus
514 lower symmetry, structures. Similarly, the radial bond distance does not show the
515 correct clustering of bond lengths as expected from an ordered structure, indicating
516 the amorphous nature of our fit. Finally, the CN distribution shows the largest
517 discrepancy at CN=12, again due to the amorphous nature of the fit. Overall, the
518 structural metrics beyond the PDF indicate the poor agreement between the final
519 and target structures. A higher simulation temperature, potentially combined with
520 CN or bond length aware potentials (such as DFT or EXAFS derived PESs) may
521 help to resolve this discrepancy.

522 **Marks decahedron**

523 The starting structure, a Marks Decahedron, was generated by the ASE Cluster tool
524 with 2 atoms on the [100] face normal to the 5-fold axis, 3 atoms on the [100] plane
525 parallel to the 5-fold axis and, 1 atom deep Marks reentrance. This produced a
526 structure with 101 atoms which was extended by one more Au atom to fill out the
527 Au_{102} structure.

528 R bounds and Q resolution were the same as the previous case. The simulation
529 ran for approximately 2.5 hours over a total of \sim 90 thousand configurations. The
530 results of the simulation are shown in Fig. ??.

531 The starting structure of Marks decahedron ($Rw=56.6\%$, see Fig. S5) yielded
532 a better structural solution, with a final Rw of 3.3%. However, the discrepancies at
533 high R remains as in the previous case. By examining the final structure, we can see
534 that these high R errors are due to a lack of the two 20-atom caps and 13 equatorial
535 atoms. Similarly, the radial bond distance distribution displays a diffusive behavior
536 unlike the bond length clustering in the target structure. Compared to the previous
537 case, the agreement in the CN and bond angle distributions are improved, with the

538 latter capturing nearly all peaks in the target structure with the exception of the 110
539 bond angle. Relatively large discrepancies are found in the CN distribution at the
540 low and high ends.

541 **Au147**

542 **3.2 PDF WITH ADPs**

543 **ADP 50**

544 1. Basic 50% larger magnitude

545 2. Random addition to APDs

546 3. Janus ADPs

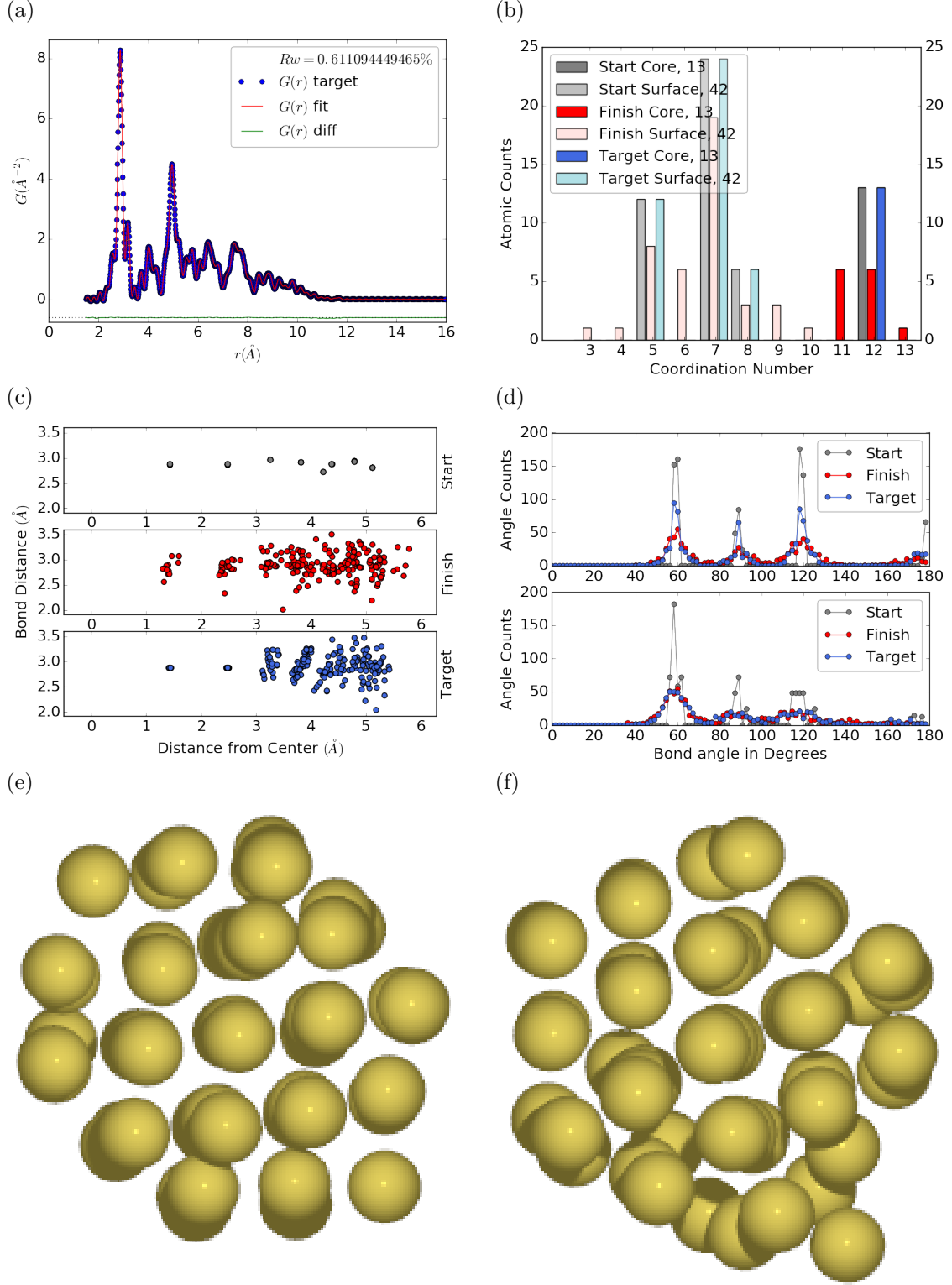


Figure 3.2: Au_{55} PDF fitting of surface-disordered Au_{55} . a) the target structure, b) the final structural solution ($R_w=0.6\%$), c) the comparison of PDFs, d) the CN distribution with the number of atoms in either the core or the surface, e) the radial bond distribution, and f) the bond angle distribution.

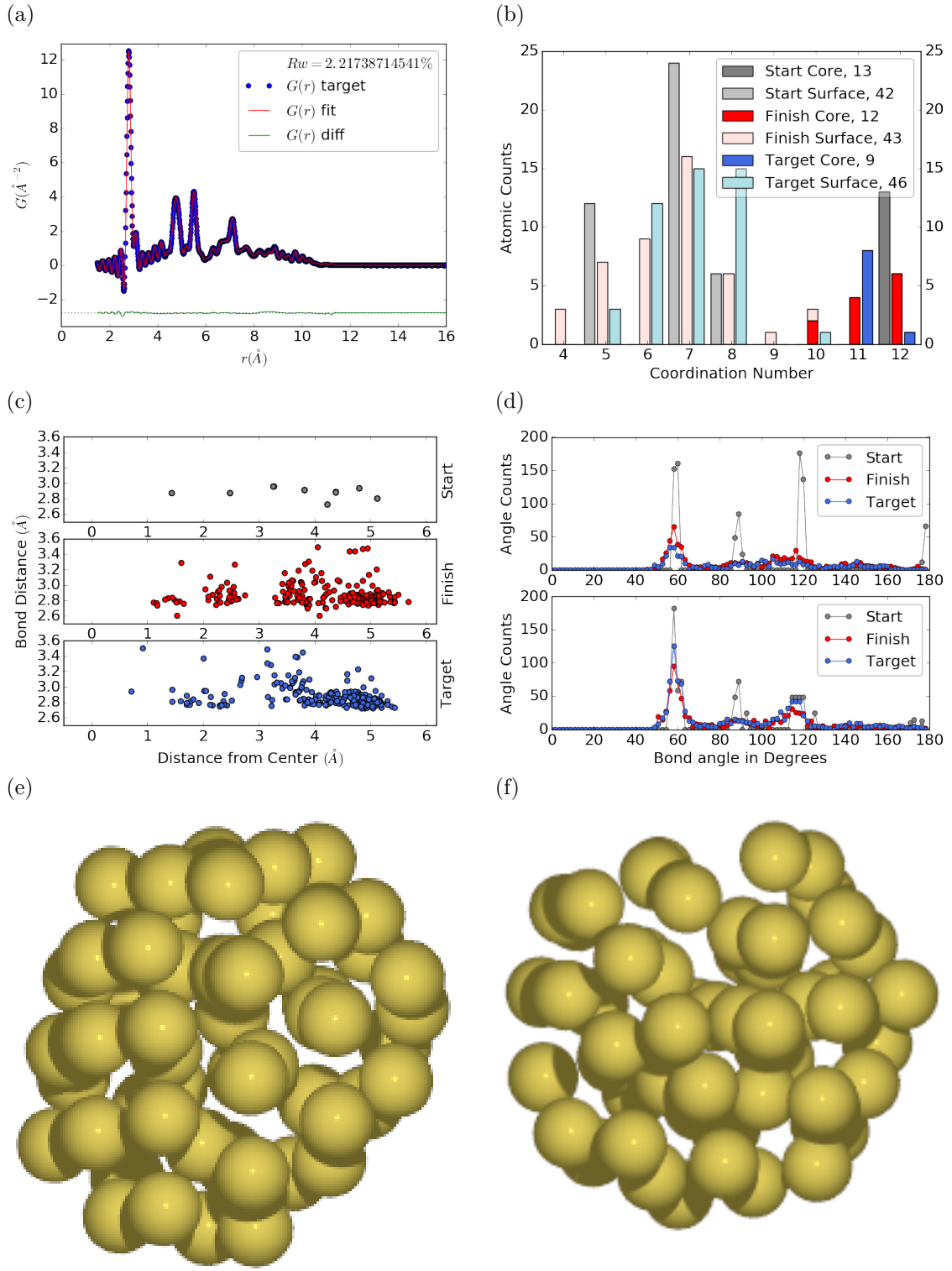


Figure 3.3: Similar to figure 3.2 for DFT-optimized amorphous Au₅₅.

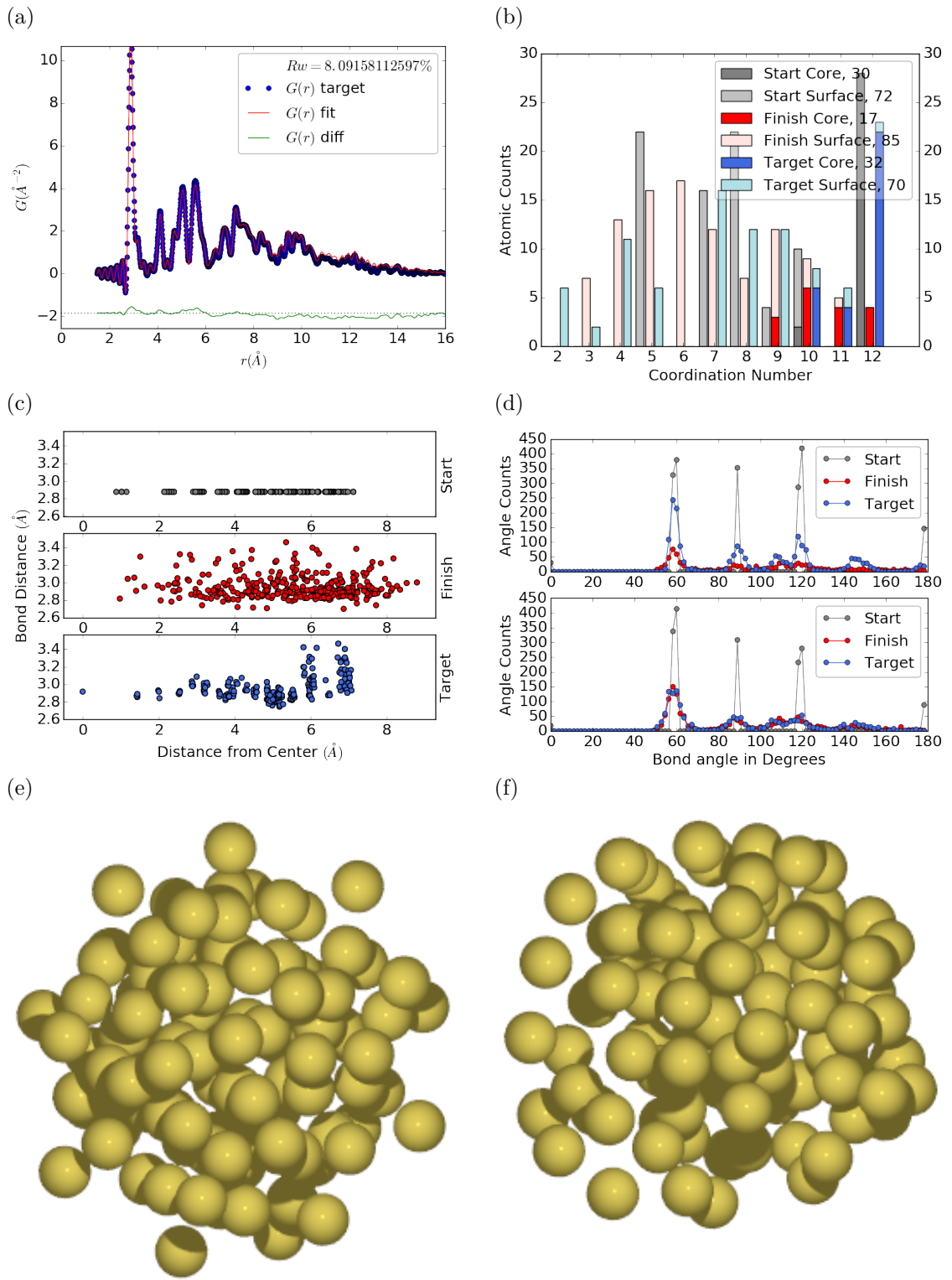


Figure 3.4: Similar to figure 3.2 for Au_{102} as in DFT-optimized $\text{Au}_{102}\text{MBA}_{44}$ cluster.

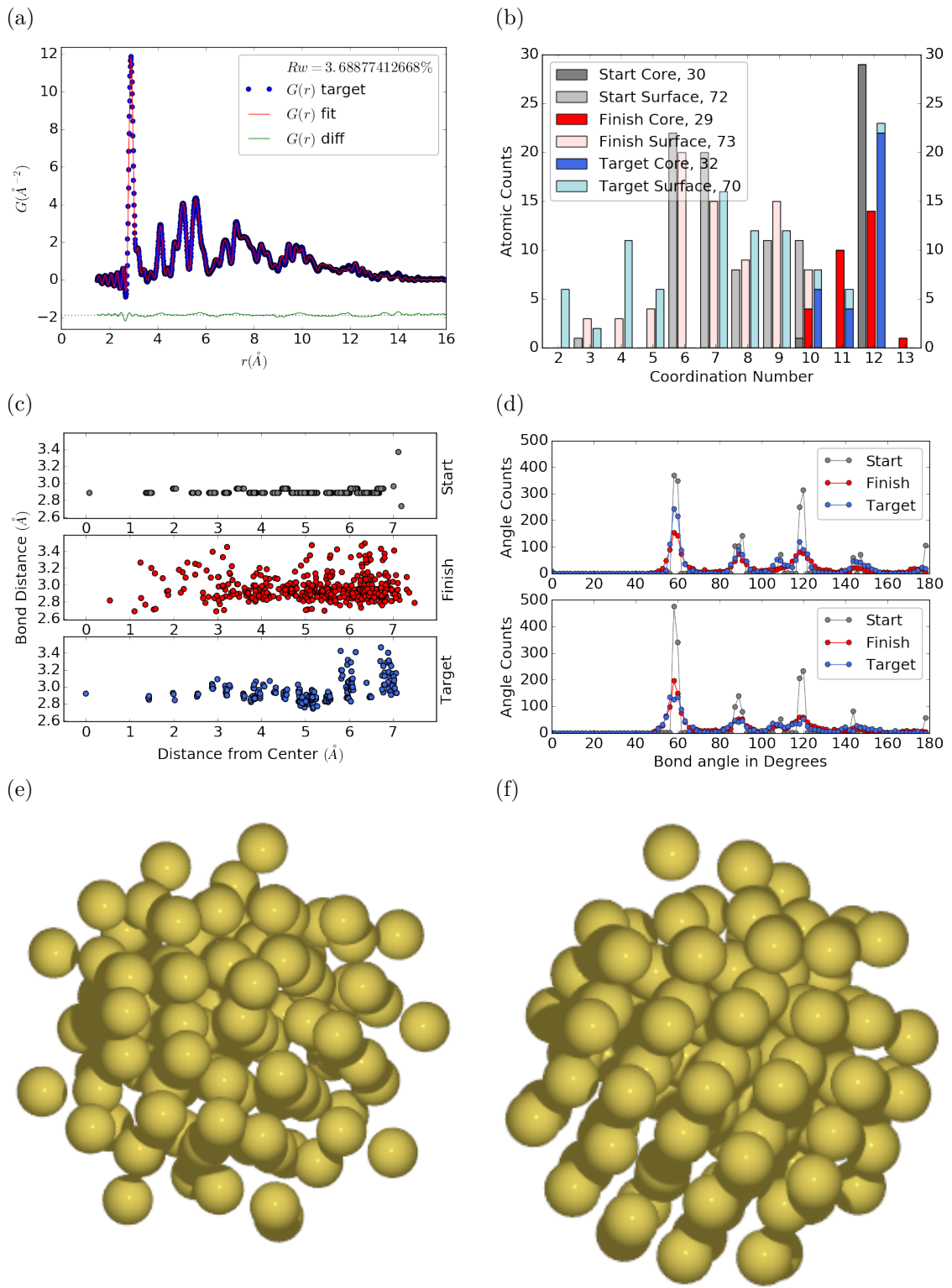


Figure 3.5: Similar to Fig. 3.6 with Marks decahedron as the starting structure.

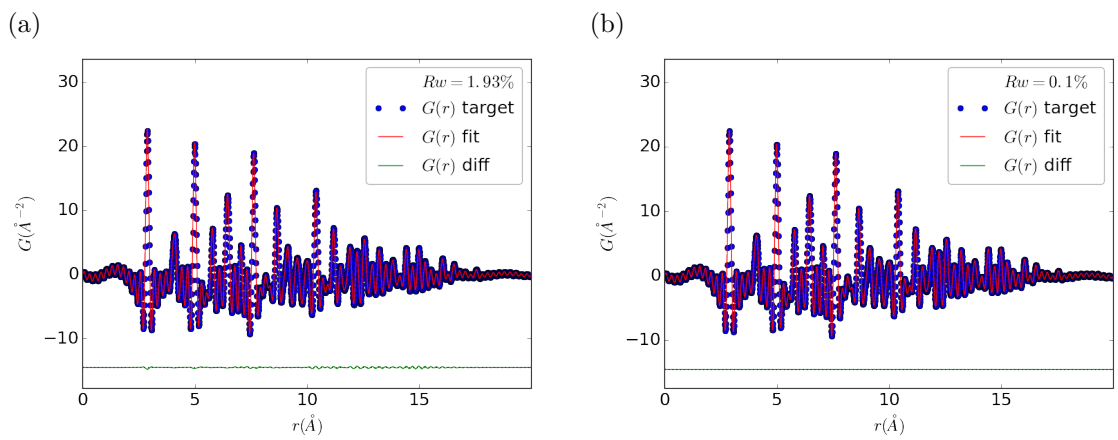


Figure 3.6

547

CHAPTER 4

548

X-RAY TOTAL SCATTERING DATA AQUESITION AND

549

PROCESSING

550 4.1 INTRODUCTION

551 X-ray total scattering experiments are generally performed at synchrotron light sources,
552 as only these sources can provide the needed flux, energy, and high momentum trans-
553 fer vectors needed to obtain reliable PDFs. [?, ?] Despite the need for a dedicated
554 facility to perform the total scattering experiments, the experiments themselves are
555 fairly forgiving, allowing for reactive gasious environments, experiment temperatures
556 ranging from 2 K to 1200 K, and even electrochemical cycling. [?, 15, ?] The rapid
557 PDF data aquesition associated with 2D area detectors creates a data management
558 problem, as 96 hours of beamtime could result in almost 10,000 images which need
559 to be associated with the experimental conditions and detector metadata. [?] Finaly,
560 all this data needs to be processed by masking bad pixels and regions, integrating
561 azimuthally, and converting the scattering data to the PDF. [?, ?, ?, ?, ?]

562 4.2 DETECTOR Q RESOLUTION

563 To properly azimuthaly integrate the images taken from the detector the Q resolution
564 of the pixels must be calculated. Integrating using even bins will cause pixels which
565 are not on the same ring to be binned together, causing the incorrect value of $I(Q)$
566 to be obtained and a larger standard deviation in the integrated data. To properly
567 calculate the Q resolution the resolution of each of the pixels in 2θ must be calculated.

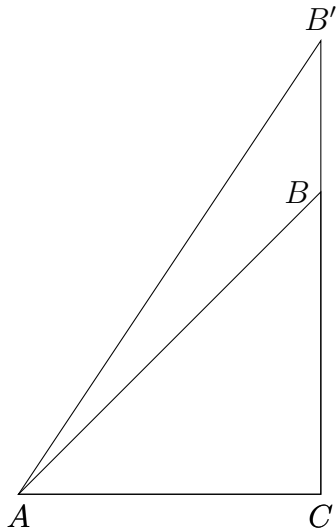


Figure 4.1: Scattering onto a flat detector

568 Figure 4.1 shows the scattering of x-rays onto a flat image plate detector. In this
 569 diagram the bottom of the n th pixel is B while the top is B' . The resolution of this
 570 pixel in 2θ is $\angle BAC - \angle B'AC$. Thus the resolution, calculated from the distances is

$$\Delta 2\theta = \arctan \frac{b}{d} - \arctan \frac{t}{d} \quad (4.1)$$

571 where d is the sample to detector distance, b is the distance to the bottom of a pixel,
 572 and t is the distance to the top of that pixel. Note that these distances need to have
 573 been corrected for detector tilt and rotation. Thus the resolution of a pixel in Q is

$$\Delta Q = \frac{4\pi(\sin \arctan \frac{b}{d} - \sin \arctan \frac{t}{d})}{\lambda} \quad (4.2)$$

574 where λ is the x-ray wavelength.

575 For a Perkin Elmer image plate, like the one used at the NSLS-II's XPD and the
 576 APS's 11-ID-B, the resolution function is shown in 4.2. For the same detector the
 577 number of pixels per Q is shown in 4.3

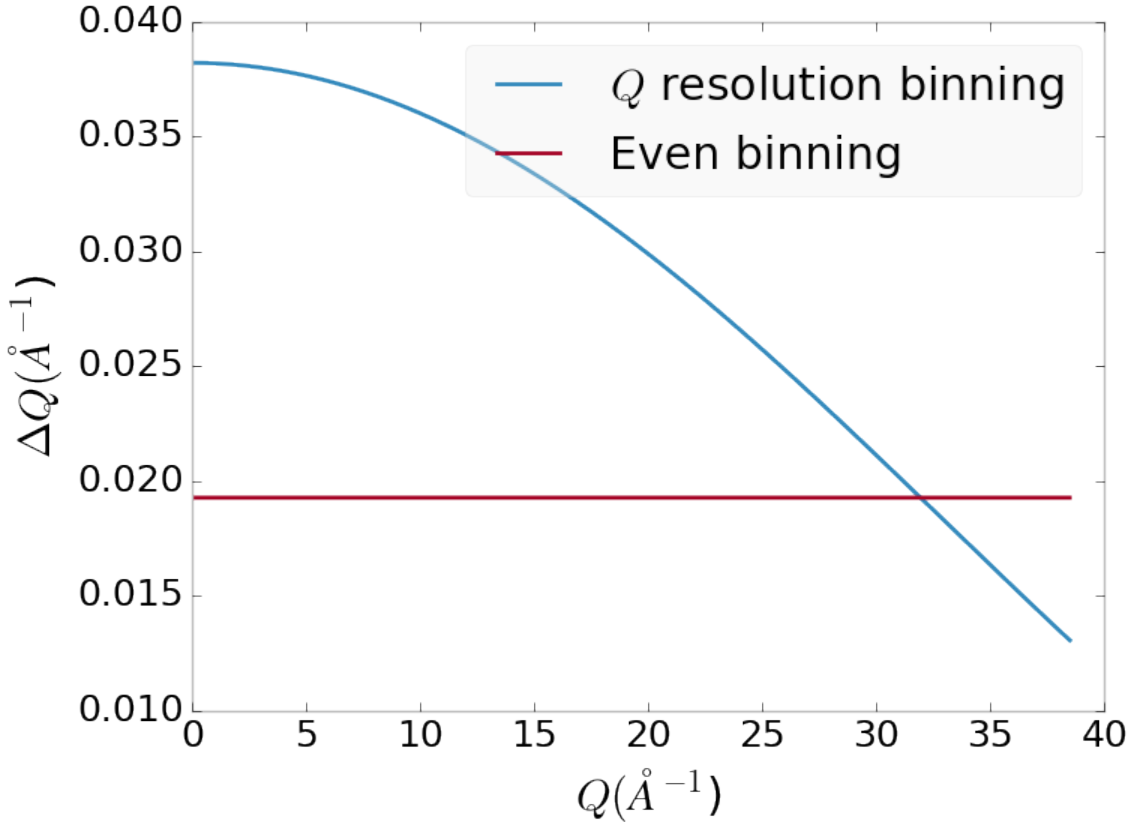


Figure 4.2: Q resolution as a function of Q .

578 4.3 AUTOMATED MASK GENERATION

579 **Introduction**

580 Detector masking is an important part of any x-ray scattering workflow as dead/hot
 581 pixels, streak errors, and beamstop associated features can be averaged into the data
 582 changing the signal and its statistical significance. While some features, like the
 583 beamstop holder, can be easily observed and masked by hand other are much more
 584 difficult to observe even on large computer monitors. Additionally, while dead/hot
 585 pixels and streaks are usually static the hot pixels associated with textured or sin-
 586 gle crystal scattering or cosmic rays are not. Thus, coming up with an automated
 587 method for finding such erroneous pixels is important, especially as high flux diffrac-
 588 tion beamlines can generate data very quickly.

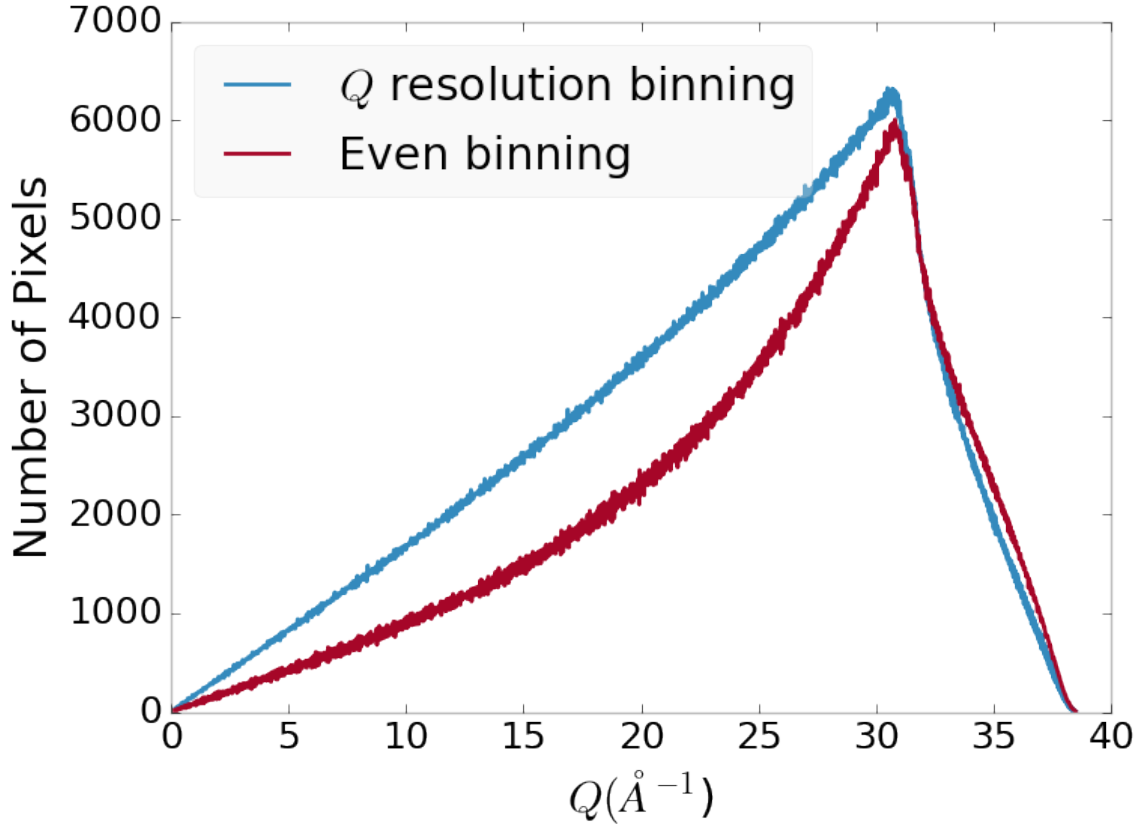


Figure 4.3: Number of pixels as a function of Q , binned at the Q resolution of the detector.

589 While this problem can be quite complex in the most general case, we can use the
 590 annular symmetry of the powder scattering pattern to our advantage, by comparing
 591 a pixel against pixels in the same ring. Since non-textured powder scattering should
 592 produce the same pixel intensity for a given ring we can mask any pixels which are α
 593 standard deviations away from the mean. This method relies on the aforementioned
 594 pixel binning algorithm, as using miss sized bins will cause some pixels which should
 595 be in separate rings to be put together, and others which should be in the same ring
 596 to be separated. In that case the masking algorithm will overestimate the number of
 597 pixels to be masked due to the additional statistical variation in the sample.

598 **Algorithm Design**

599 The masking algorithm procedure takes in the image and a description of the pixel
600 positions in either distance from the point of incidence or in Q . The image is then
601 integrated twice, producing both the mean $I(Q)$ and the standard deviation of each
602 $I(Q)$ ring. The mask is created by comparing the pixel values against each ring's
603 standard deviation and threshold α . Note that the threshold can be a function of
604 distance from the point of incidence or Q .

605 **Test Cases**

606 To study the effectiveness of the masking we ran the algorithm against both simulated
607 experimental data. In the case of the simulated data four systems were created: 1)
608 dead/hot pixels with varying numbers of defective pixels, 2) beamstop holder with
609 varying beamstop holder transmittance, 3) rotated beamstop holder with varying
610 beamstop holder transmittance, and 4) beamstop holder with dead/hot pixels. The
611 base scattering was produced by

$$I = 100 \cos(50r)^2 + 150 \quad (4.3)$$

612 where r is a pixel's distance from the beam point of incidence. The positions of
613 the dead/hot pixels were chosen at random as was the dead or hot nature of the
614 defect. Dead pixels had values from 0 to 10, while hot pixels had values from 200
615 to 255. The beamstop was positioned at the vertical center of the detector with an
616 initial width of 60 pixels and final width of 120 pixels. The height of the beamstop
617 was 1024 pixels. The beamstop was calculated to attenuate the x-ray scattering
618 signal at various transmittance, as various beamstop holder materials have different
619 transmittance. Two versions of the masking algorithm were run for each test case, one
620 using the standard even bin sizes for the integration step, and one where the bin sizes
621 are tuned to the pixel Q resolution as discussed in 4.2.

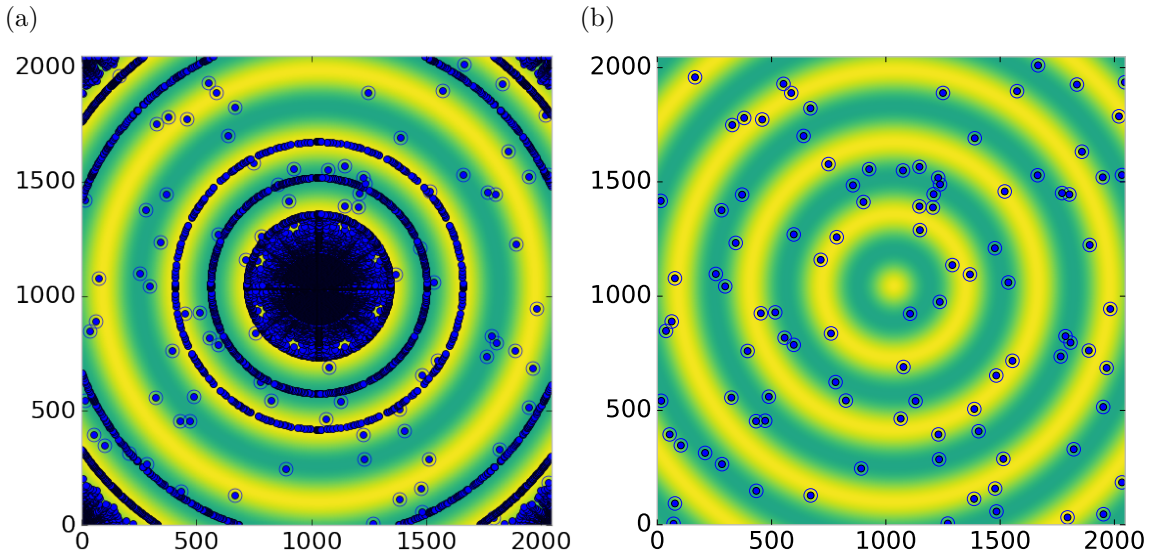


Figure 4.4: Generated dead/hot pixel masks for a detector with 100 bad pixels. a) the standard even bin mask and b) the Q resolution binned mask. The bad pixels are noted with open circles, masked pixels are noted with closed circles.

622 Results and Discussion

623 Figures 4.4-4.11 show the results of the masking algorithm on simulated images. The
 624 dead/hot pixel masking shows the importance of using the Q resolution based bin sizes
 625 as the even bin based mask have a tendency to over mask the image, removing pixels
 626 which contain valuable signal. This overmasking is caused by pixels being improperly
 627 associated with one another by the even bins. Figure 4.4 indicates that the masking
 628 algorithm, with the proper binning, masks the image perfectly, with no missed bad
 629 pixels or good pixels masked. This is not the case in figures 4.5 - 4.7 as we can see
 630 pixels which should have been masked but were not. Despite these missed pixels no
 631 pixels were improperly masked in any of the well binned images. These test cases
 632 are actually more difficult than experimental data, as the dynamic range of most
 633 detector causes the dead/hot pixels and single crystal/textured peaks to be orders of
 634 magnitude away from the desired signal.

635 The beamstop holder masks shown in figures 4.8 - 4.11, which were all run with

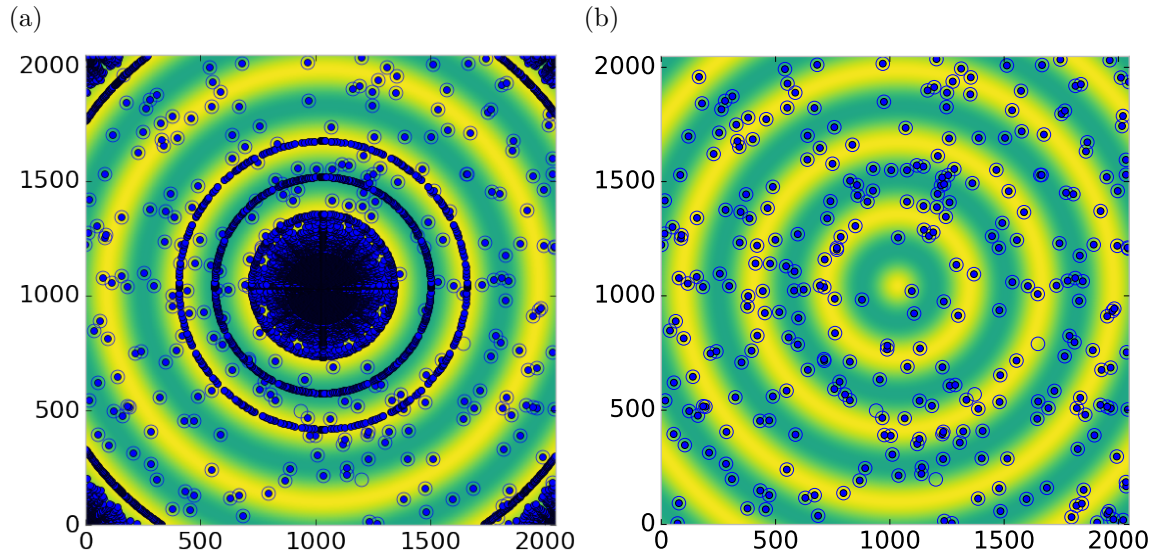


Figure 4.5: Generated dead/hot pixel masks for a detector with 300 bad pixels. a) the standard even bin mask and b) the Q resolution binned mask. The bad pixels are noted with open circles, masked pixels are noted with closed circles.

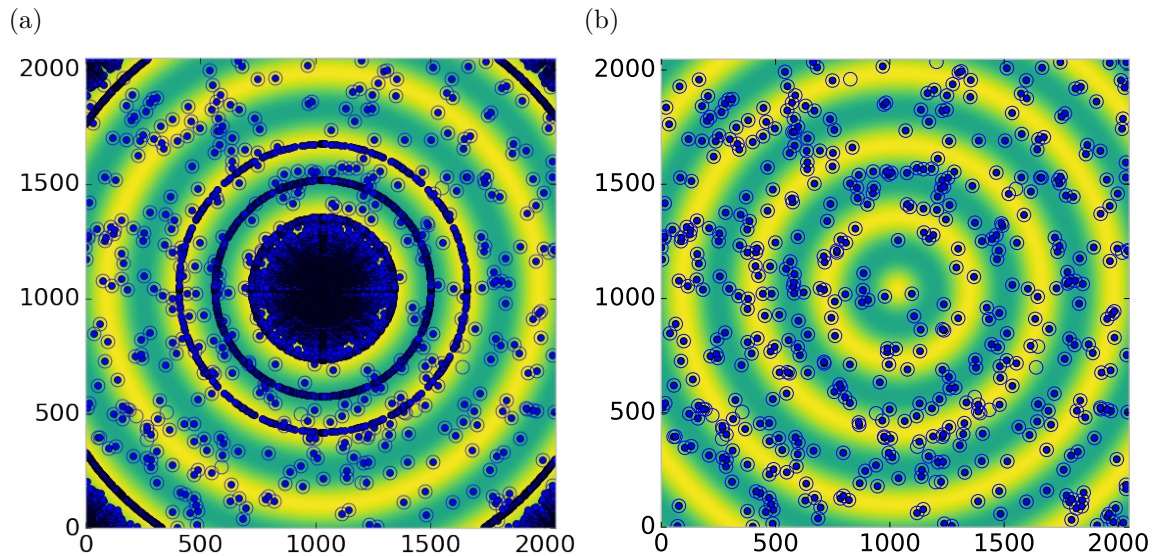


Figure 4.6: Generated dead/hot pixel masks for a detector with 500 bad pixels. a) the standard even bin mask and b) the Q resolution binned mask. The bad pixels are noted with open circles, masked pixels are noted with closed circles.

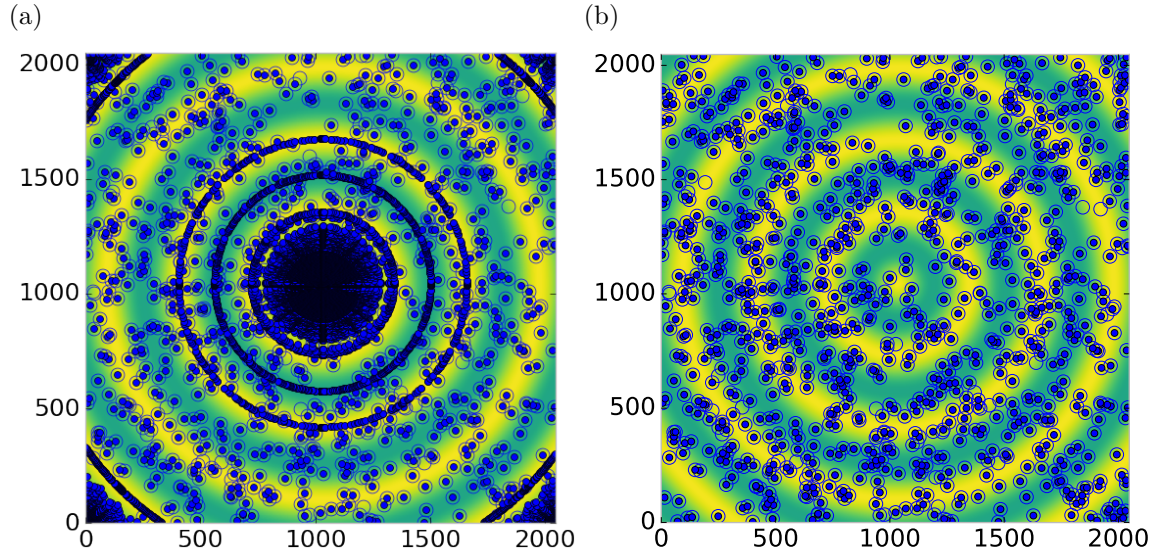


Figure 4.7: Generated dead/hot pixel masks for a detector with 1000 bad pixels. a) the standard even bin mask and b) the Q resolution binned mask. The bad pixels are noted with open circles, masked pixels are noted with closed circles.

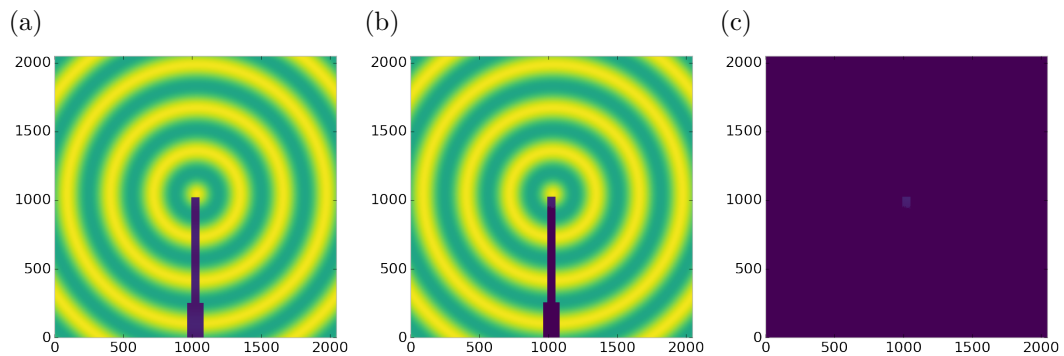


Figure 4.8: Generated beamstop holder masks for a beamstop holder with 10% transmittance. a) the raw image, b) the masked image, c) and the missed pixels

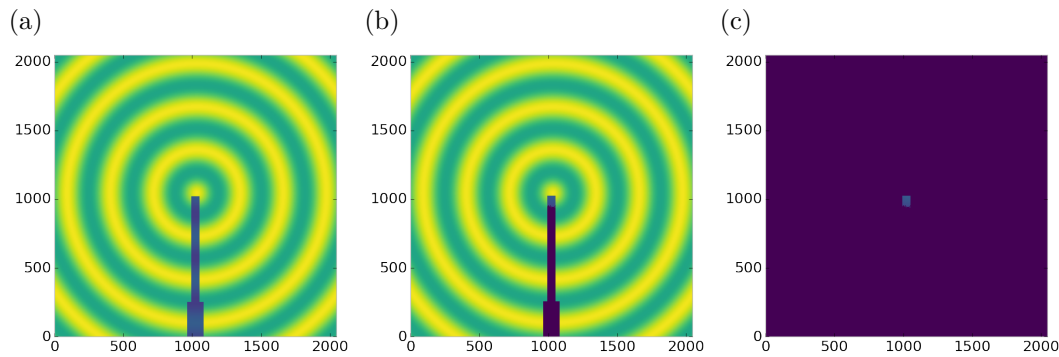


Figure 4.9: Generated beamstop holder masks for a beamstop holder with 30% transmittance. a) the raw image, b) the masked image, c) and the missed pixels

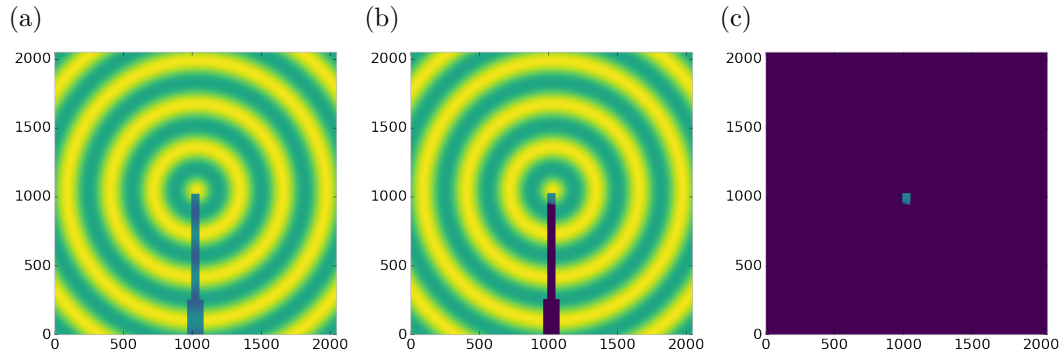


Figure 4.10: Generated beamstop holder masks for a beamstop holder with 50% transmittance. a) the raw image, b) the masked image, c) and the missed pixels

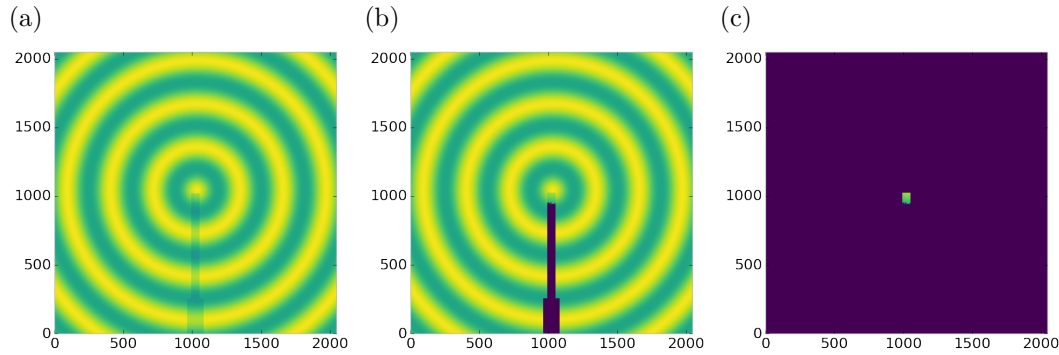


Figure 4.11: Generated beamstop holder masks for a beamstop holder with 90% transmittance. a) the raw image, b) the masked image, c) and the missed pixels

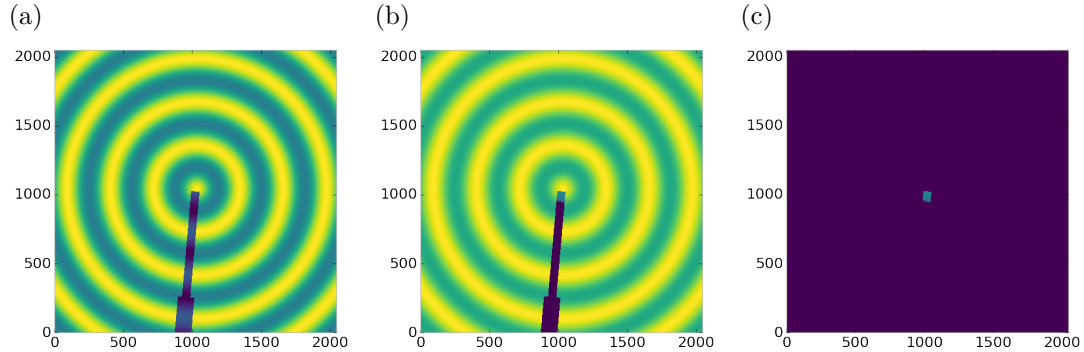


Figure 4.12: Generated beamstop holder masks which is rotated away from verticle

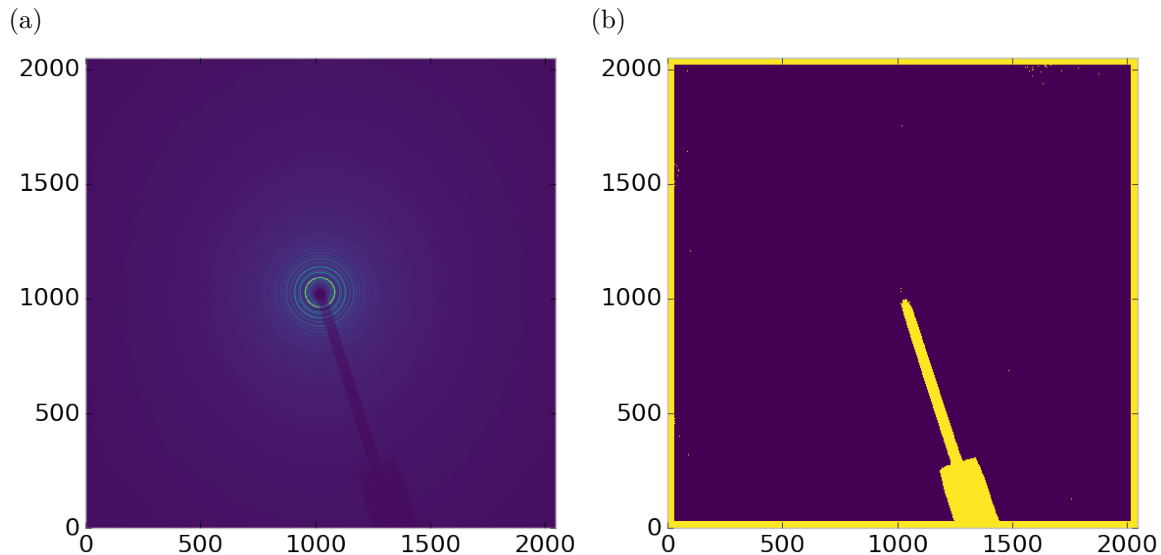


Figure 4.13: Masked experimental data. a) the raw image, b) the mask

the Q resolution binning show similar results across the transmittance range, missing only a small part of the beamstop holder near the point of incidence. Near this point the beamstop holder becomes a statistically significant part of the total number of pixels in a given ring, thus it can not be masked out using a statistical search of the rings. For most PDF and XRD studies this small area can be masked automatically by masking all the pixels who's distance from the point of incidence is smaller than a given radius r , or can be negelected outright as the area is not used in the analysis or refinement. Similar results were produced for beamstop holders which were rotated away from the vericle position, as shown in figure 4.12

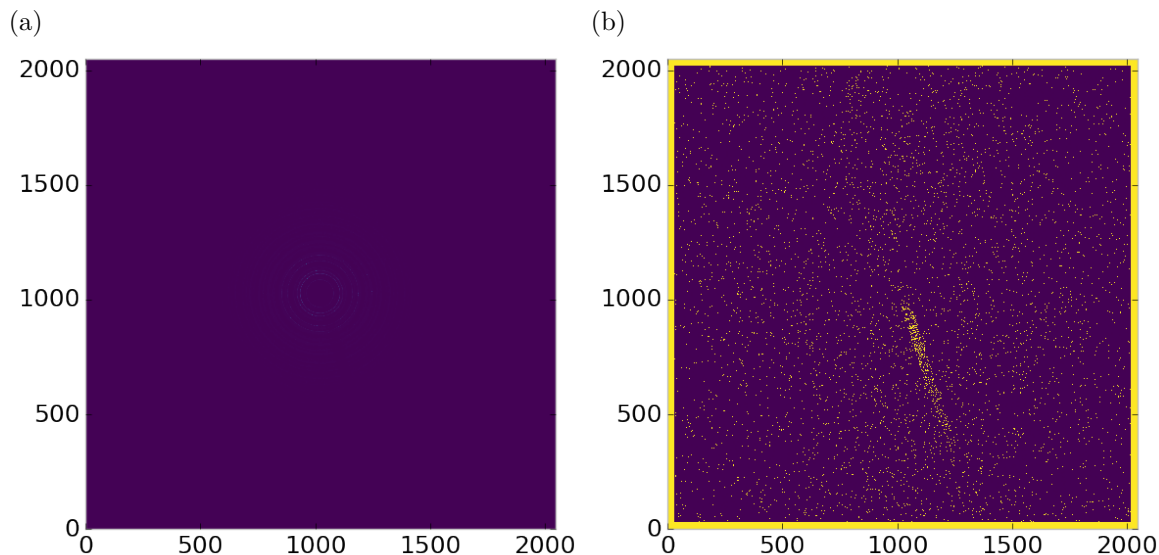


Figure 4.14: Masked experimental data with Pt single crystal signal. a) the raw image, b) the mask

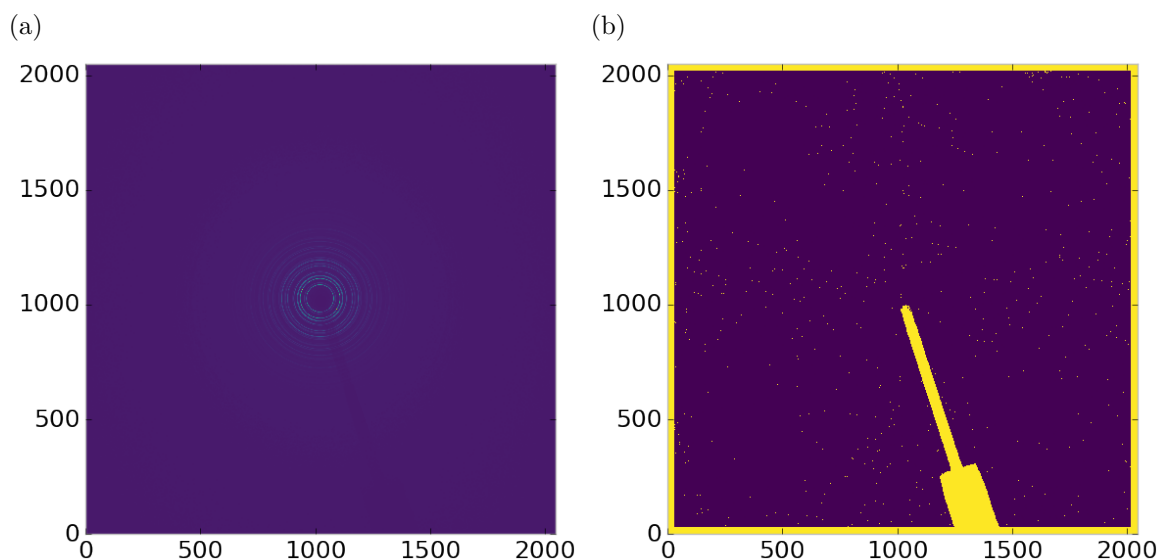


Figure 4.15: Masked experimental data with Pt single crystal signal using figure's 4.13 as a starting mask. a) the raw image, b) the mask

Working with actual experimental data, obtained at the Advanced Photon Source beamline 11-ID-B, shows the difficulty of masking images which have low phonon counts. While the masking of experimental data taken with longer exposures, consisting of 250 .2 second shots, shown in figure 4.13 provides very sharp edges to the beamstop holder, and very little extra masking beyond the occasional dead pixel, this is not the case for the single crystal data. The single crystal data is more problematic because of its short exposure time and low flux, with 500 frame at a .1 second exposure and having shrunk the beam size. The low flux is to prevent the very strong single crystal peaks from damaging the detector. However, this causes the image to be less statistically viable than ideal, causing problems with the mask as seen in figure 4.14. This can be alleviated to some degree by using the previously generated mask as a starting mask for the single crystal image, as shown in 4.15. While the masking algorithm still produces many diffuse masked pixels, they are far fewer, this may be due to the removal of the beamstop which could have contributed to the large standard deviation in figure 4.14.

Conclusions

In this section the masking algorithm, which relies on both Q resolution based binning and a statistical approach to azimuthal symmetry, was developed. The focus of this algorithm was to remove many unwanted detector features associated with pixel defect, beamstop holder associated scattering attenuation, and single crystal/texture peaks. Simulated data was used to evaluate the beamstop holder and dead/hot pixel masking capacity, while experimental data was used to check for single crystal and texture based masking. Q resolution based binning was shown to be very important to avoid overmasking. The ability of the mask writer to mask images is somewhat limited by the overall statistical image quality, although some deficiencies can be obtained by using previously generated masks as starting points. This masking algorithm is now

671 in use in the data processing workflow and will be available in scikit-beam soon.

672 4.4 AUTOMATED IMAGE AZIMUTHAL INTEGRATION

673 Using the Q resolution binning and masking developed in sections 4.2 and 4.3 the
674 images can be properly integrated. Generally, images are integrated by taking the
675 mean value of the pixels in a ring. However, other statistical measures of the average
676 value can be used, like the median.

677 Figures 4.16-4.18 show the importance of masking and the choice of average function.
678 All the figures were produced using the same dataset, 50 °C Pr_2NiO_4 taken at
679 the APS's 11-ID-B on a Perkin Elmer area detector. The automatic masking alpha
680 was 3 standard deviations from the mean. While it is difficult to observe the changes
681 the mask causes in the full $I(Q)$ plot (subfigures a) and b)), the standard deviation
682 plots show the effect of bad pixels on the data (subfigure c)). Subfigure c) for figures
683 4.16-4.18 shows that removal of the beamstop holder lowers the low Q standard de-
684 viation from around .1 to almost .01 out to 15 \AA^{-1} . The high Q subfigures d) and f)
685 in figures 4.16-4.18 show the “kink” effect of the detector edge and beamstop holder,
686 where there is a dip in the $I(Q)$ scattering when the rings include the edge of the
687 detector. This effect seems to be due to both errors in the edge pixel intensity and the
688 beamstop holder as masking of the edges only seems to provide only partial removal
689 of the issue. It is important to note that while integration using the mean of the
690 ring has issues with only the edge mask, as evidenced by the change in slope in 4.17
691 d) around 29.5 \AA^{-1} , the median integration does not include this error. Ideally the
692 detector would have a normal distribution of pixel intensity for a given ring, which
693 would imply an equivalency between the mean and median $I(Q)$ values. Despite the
694 closeness of the mean and median once the final mask has been created, it seems that
695 the median is more reliable, as it was less effected by the beamstop holder in figure
696 4.17. Thus, for subsequent integrations discussed in this work the median is used to

697 avoid any defective features that the masking algorithm may have missed.

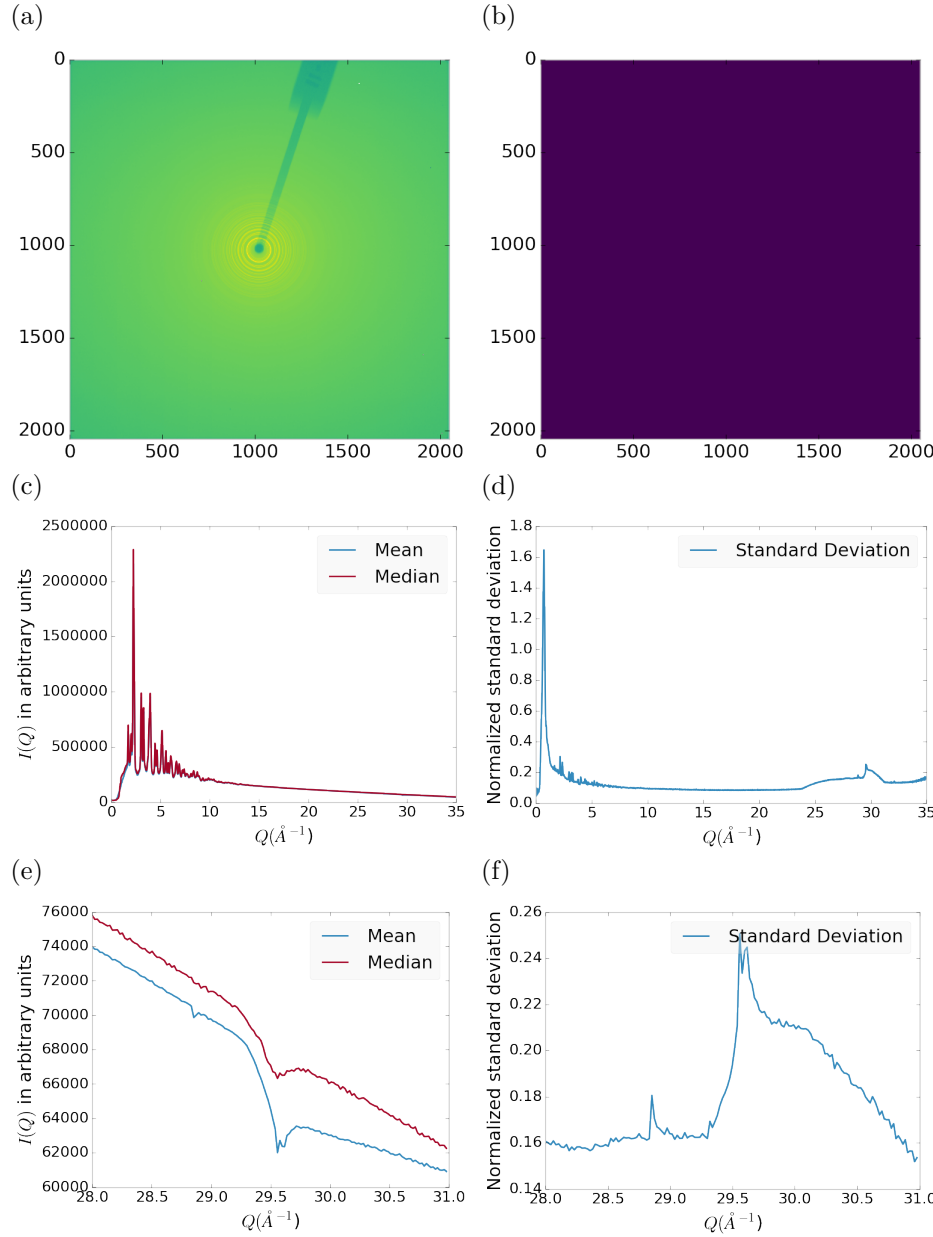


Figure 4.16: Masking, average, and standard deviation of an example x-ray total scattering measurement. This image was produced with no mask. a) the image, b) the mask, c) the mean and median values, d) the standard deviation (normalized to the median), e) a closeup of the 28 \AA^{-1} to 31 \AA^{-1} Q range for the mean and median, f) 28 \AA^{-1} to 31 \AA^{-1} Q range for the standard deviation

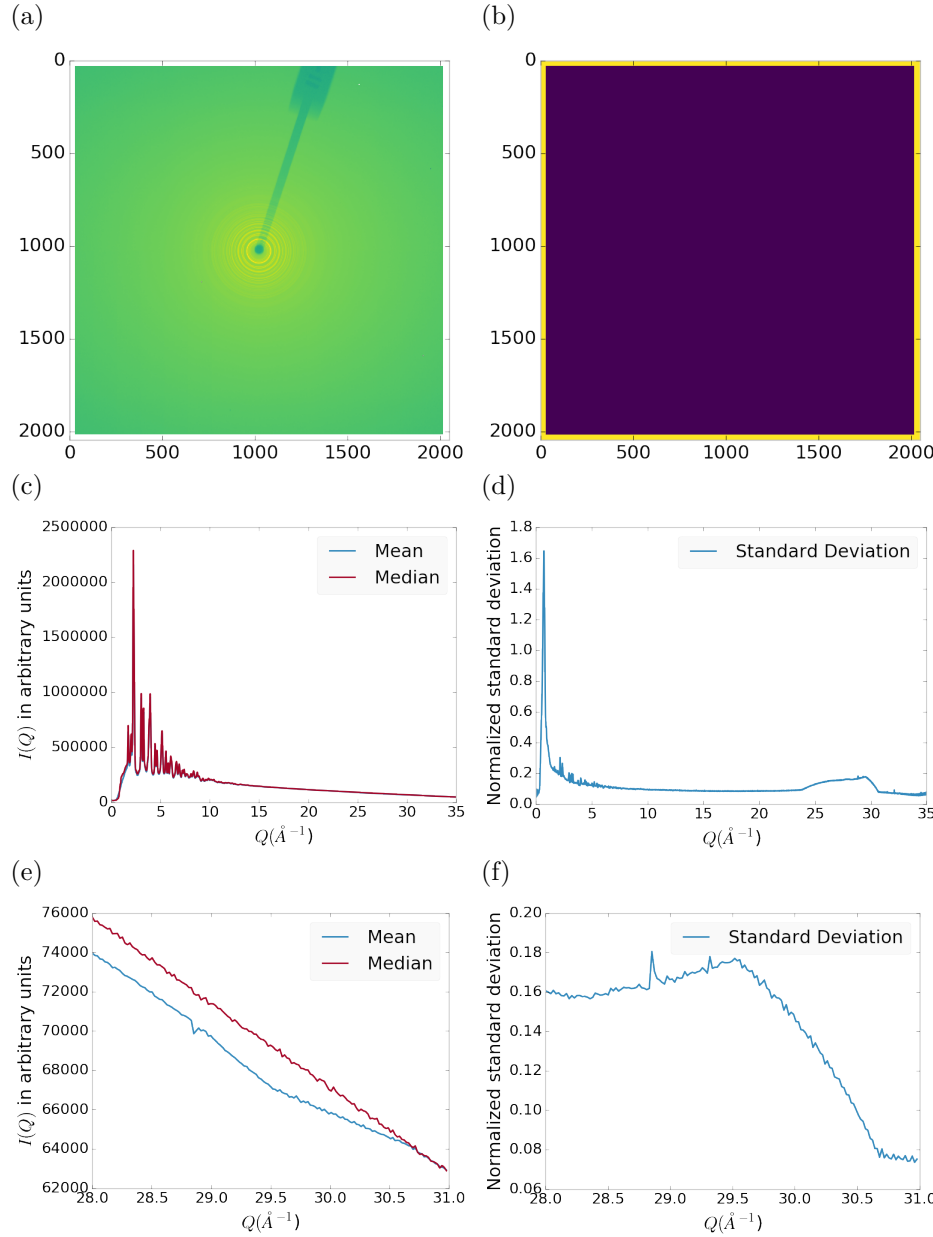


Figure 4.17: Masking, average, and standard deviation of an example x-ray total scattering measurement. This image was produced with only an edge mask. a) the image, b) the mask, c) the mean and median values, d) the standard deviation (normalized to the median), e) a closeup of the 28\AA^{-1} to 31\AA^{-1} Q range for the mean and median, f) 28\AA^{-1} to 31\AA^{-1} Q range for the standard deviation

698 4.5 CONCLUSIONS

699 This chapter developed and analyzed the proper data processing and reduction method-
 700 ology for producing reliable $F(Q)$ data from x-ray total scattering measurements.

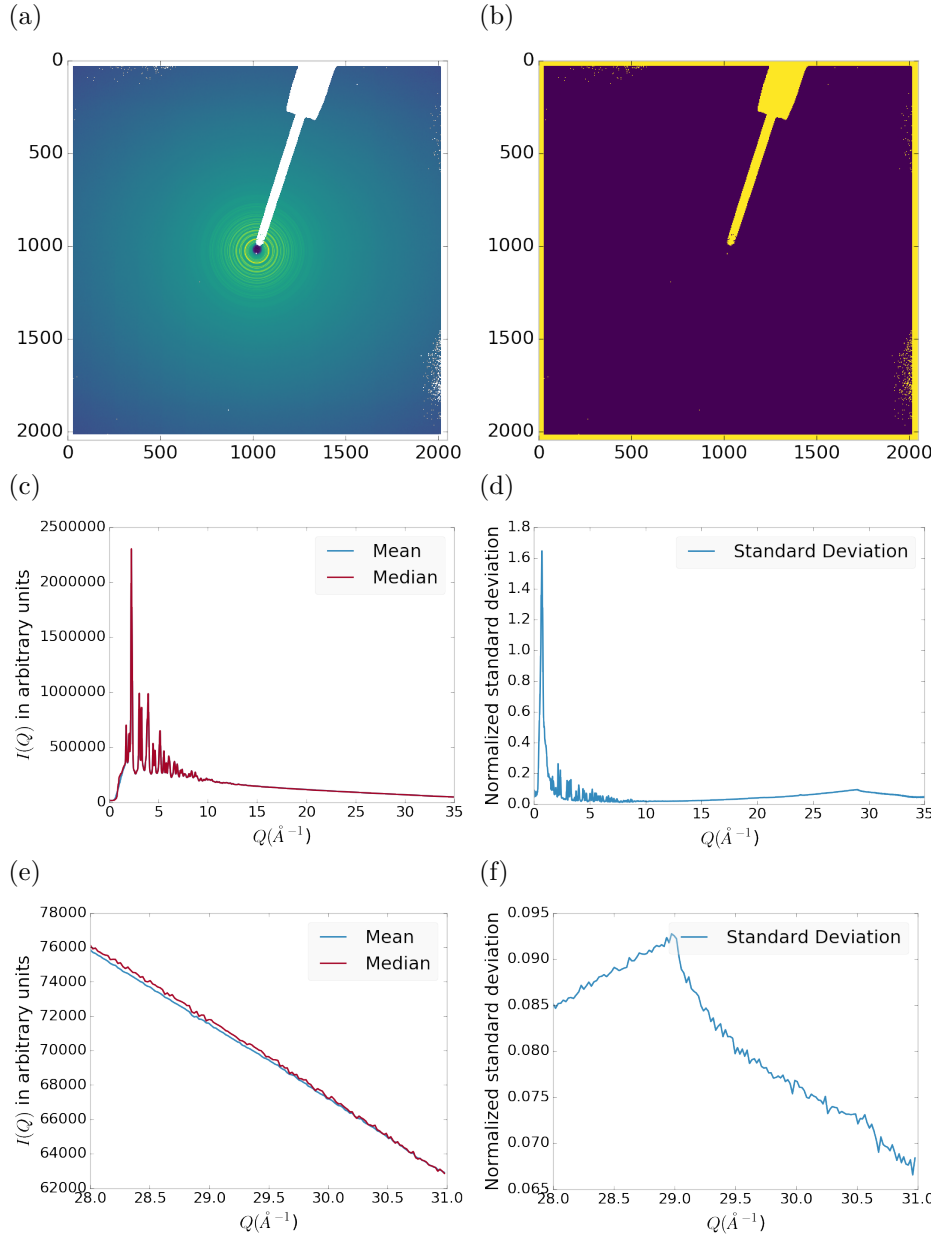


Figure 4.18: Masking, average, and standard deviation of an example x-ray total scattering measurement. This image was produced combining an edge mask and the automatically generated mask. a) the image, b) the mask, c) the mean and median values, d) the standard deviation (normalized to the median), e) a closeup of the 28 \AA^{-1} to 31 \AA^{-1} Q range for the mean and median, f) 28 \AA^{-1} to 31 \AA^{-1} Q range for the standard deviation

701 Binning at the Q resolution of the detector was found to be key to the data process-
 702 ing. The primary outcome of using the Q resolution binning was an enhancement in
 703 effectiveness for the masking algorithm, producing much fewer false positives for dead

704 pixels. This masking approach was then applied to the integration of experimental
705 data taken at the APD's 11-ID-B beamline. The automatically generated masks, when
706 combined with edge masks, were found to greatly reduce the overall standard devi-
707 ation of the pixel intensity and produce a smoother $F(Q)$ at high Q , enabling the
708 use of much higher Q data in the PDF. Different statistical measures used in the
709 azimuthal integration was also compared. This comparison showed that the median
710 was a more reliable statistic for integration with data which had more detector de-
711 fects. However, upon properly masking it was shown that these metrics were almost
712 identical. The masking induced similarity between the mean and median shows that
713 the rings, when integrated, may form a Gaussian distribution. The distribution of
714 the pixel intensities for strongly and weakly scattering samples may be investigated
715 in future work.

716

CHAPTER 5

717

ANNEALING AND AGGREGATION OF 2NM

718

AU NANOPARTICLES

719 5.1 EXPERIMENTS

720 NP Synthesis

721 X-ray Total Scattering Measurements

722 5.2 DATA PROCESSING

723 5.3 DATA ANALYSIS

724 5.4 SIMULATION

725 5.5 STRUCTURAL ANALYSIS

726 5.6 CONCLUSIONS

727

CHAPTER 6

728

PHASE CHANGES AND ANNEALING DYNAMICS OF

729

Pr_2NiO_4 AND ITS DERIVATIVES

730 6.1 EXPERIMENTS

731 **Pr_2NiO_4 Synthesis**

732 **X-ray Measurements**

733 X-ray total scattering and x-ray powder diffraction experiments were performed at
734 the APS's 11-ID-B beamline. An x-ray energy of XXX keV, YYY Å was used. The
735 detector was moved between a 20cm and a 95 cm sample to detector distance to mea-
736 sure the x-ray total scattering and x-ray diffraction patterns. Various PNO samples
737 were annealed on the beamline during x-ray measurement.

738 6.2 DATA PROCESSING

739

masking parameters

740

integration parameters

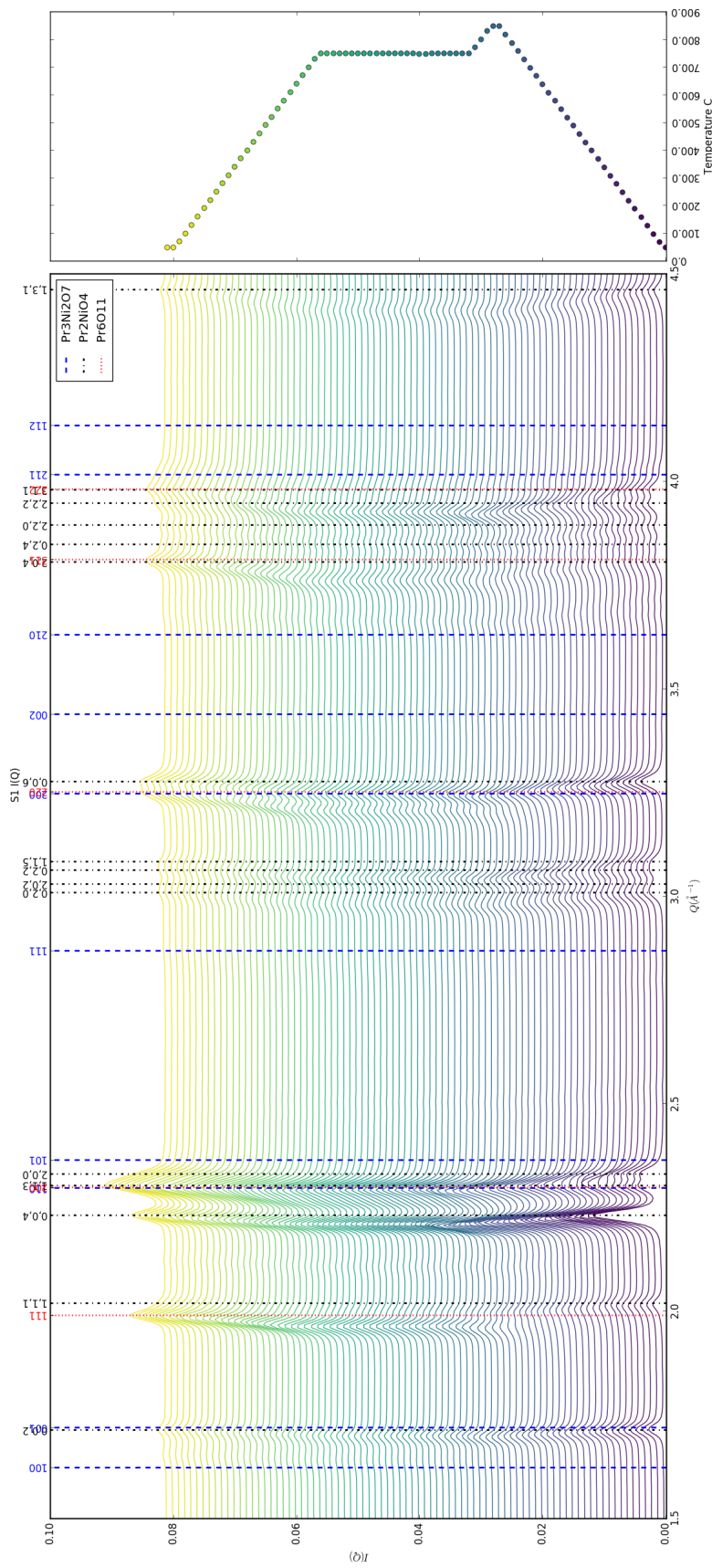
741

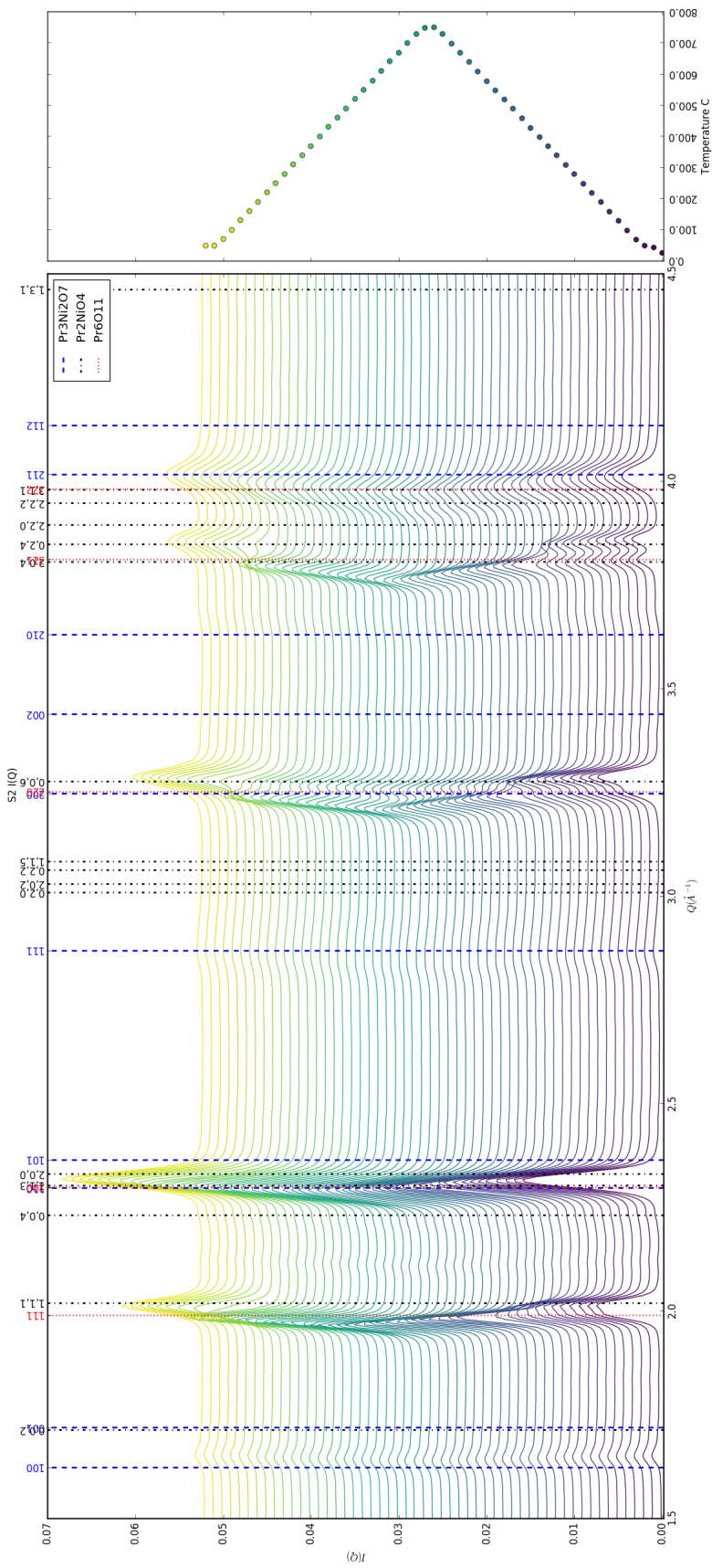
PDF parameters

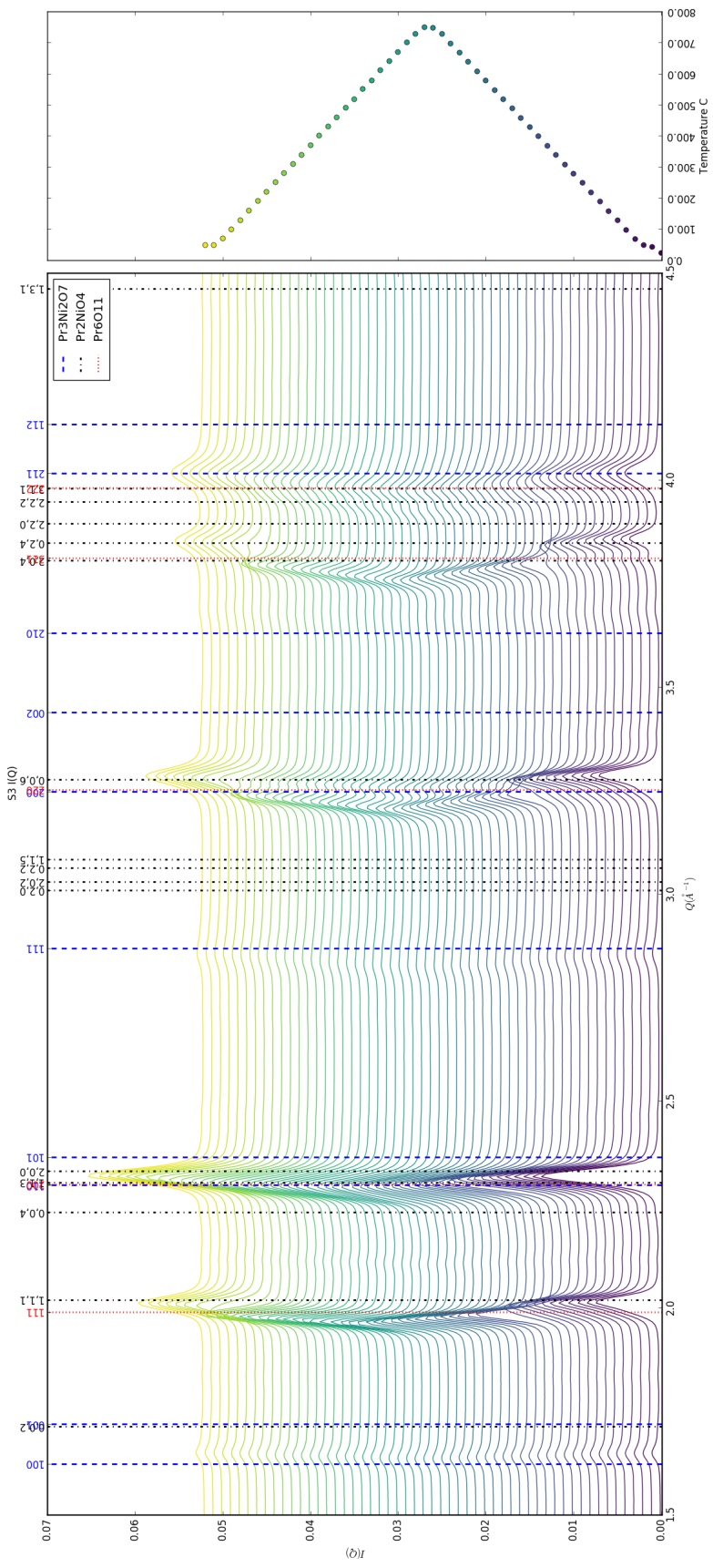
742 6.3 DATA ANALYSIS

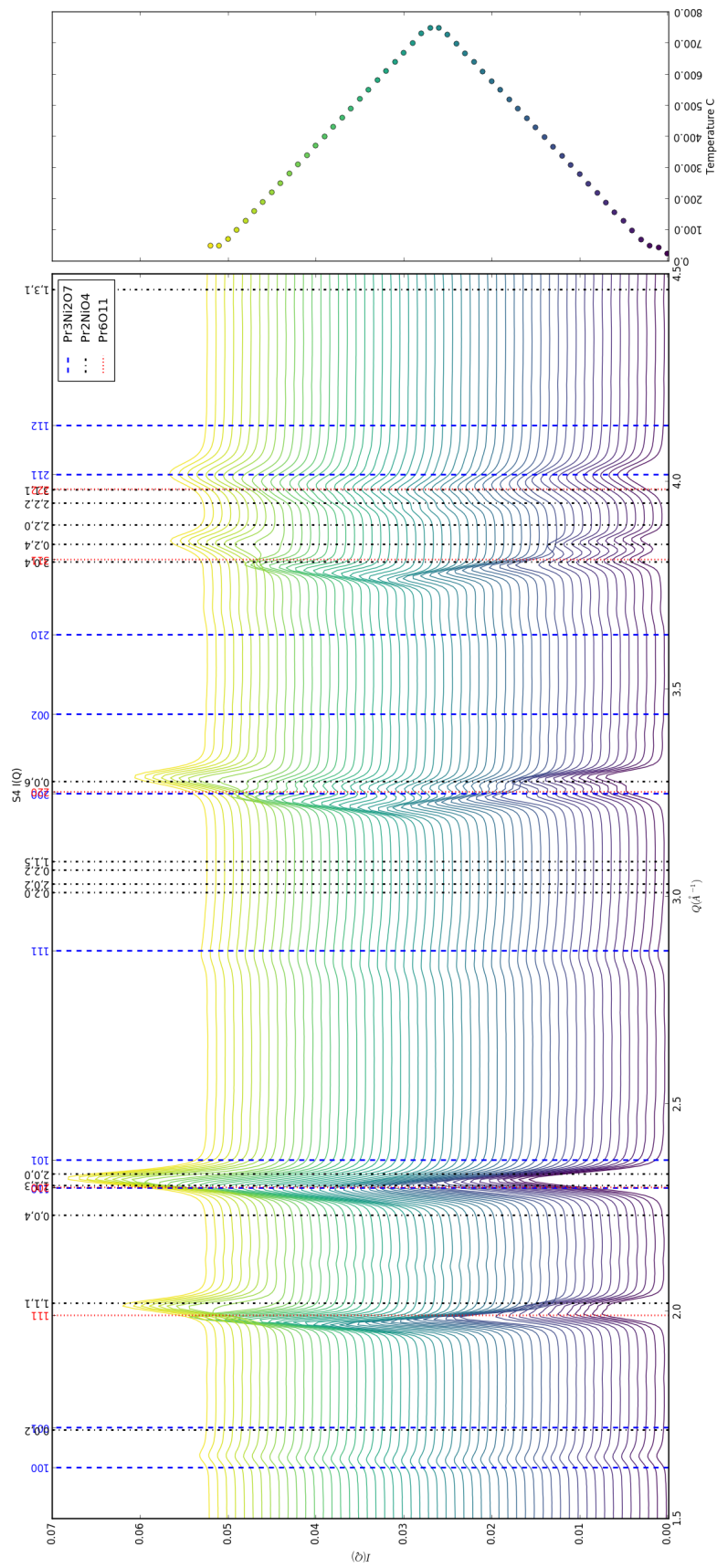
743 **Intra Sample Comparison**

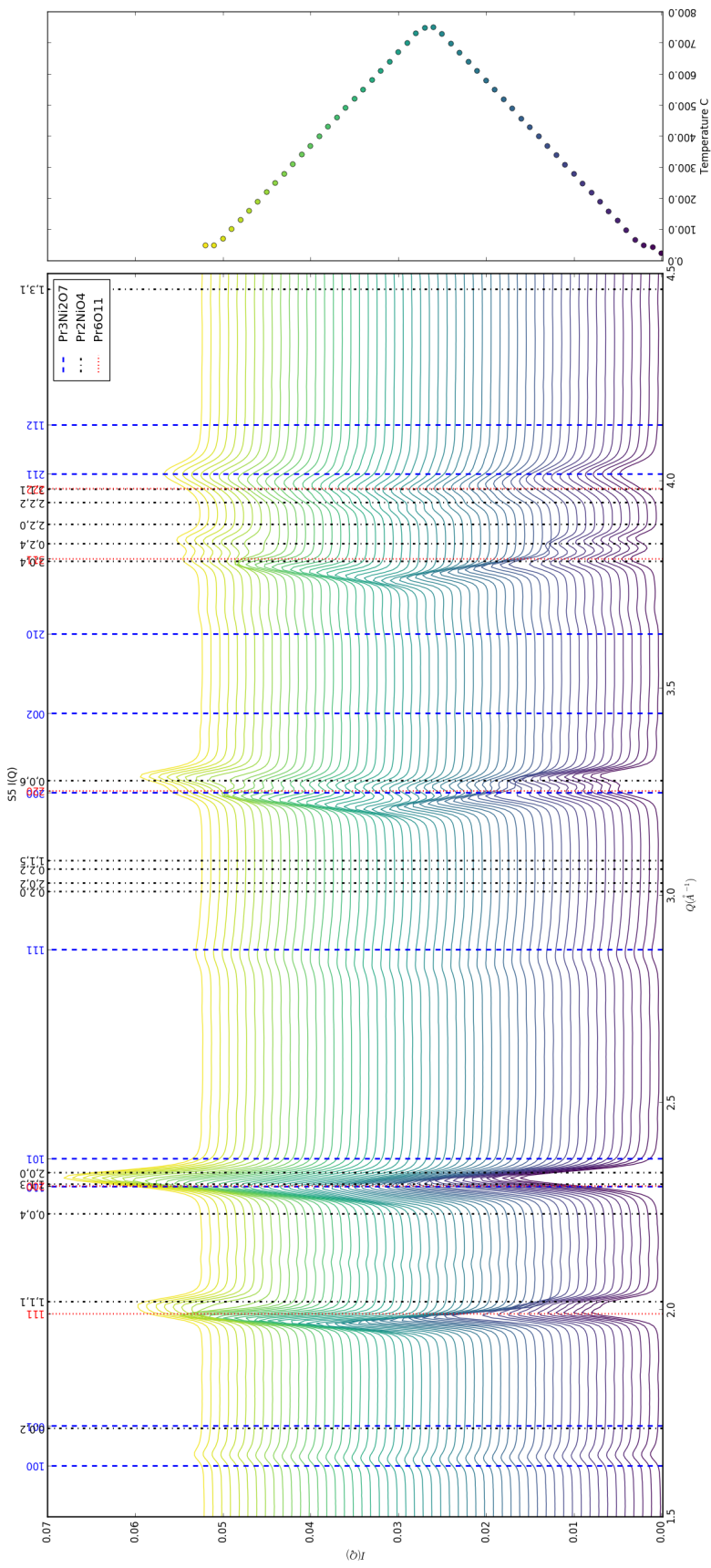
744 Changes in S1 but very little in S2-5.



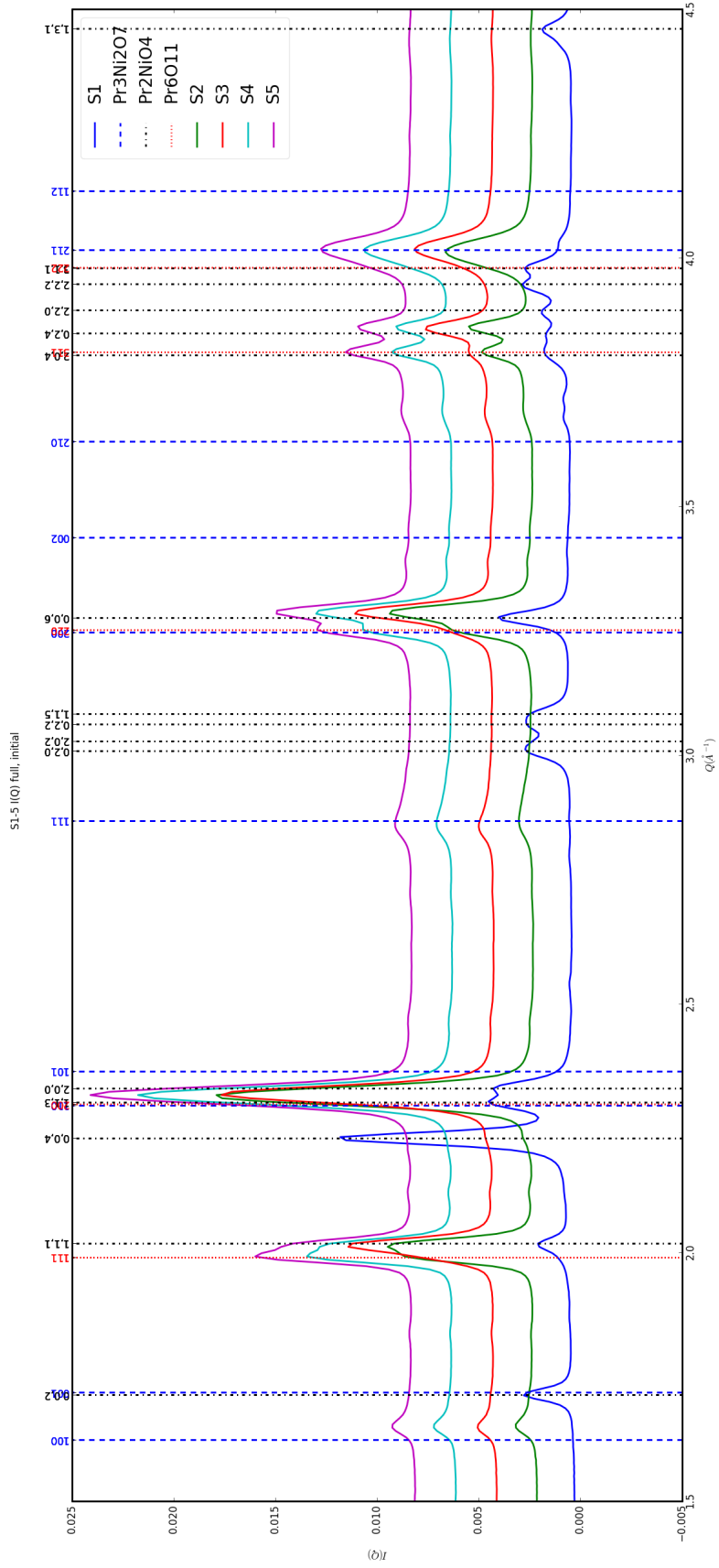


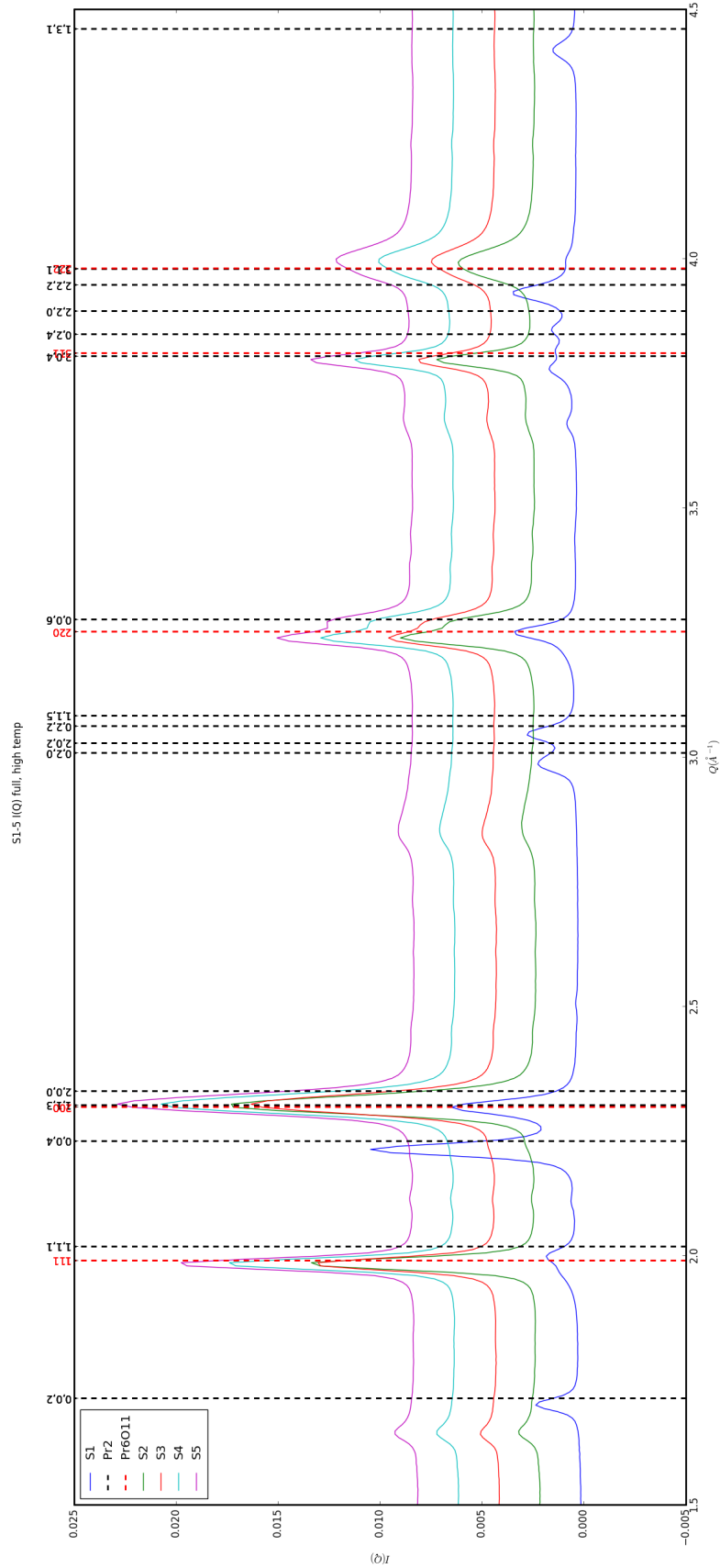


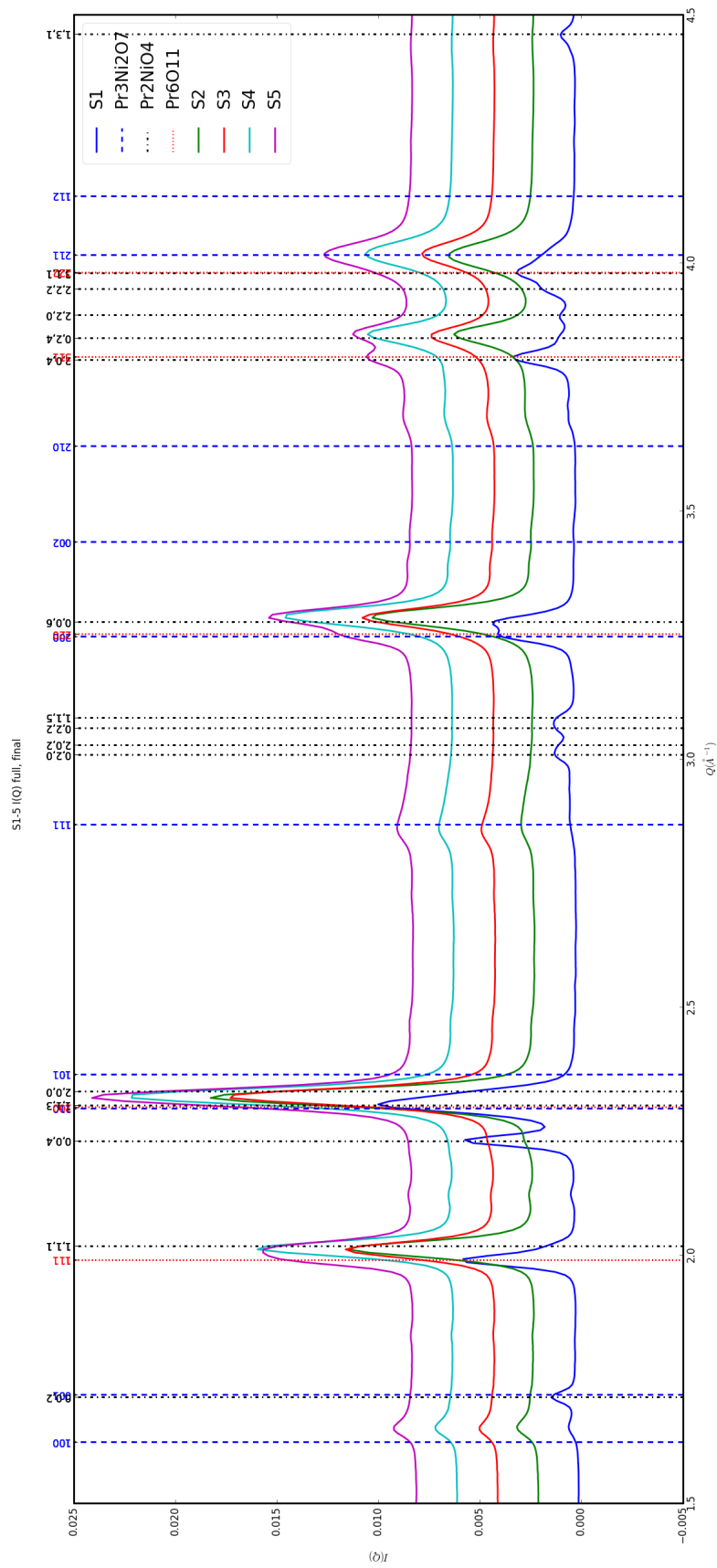


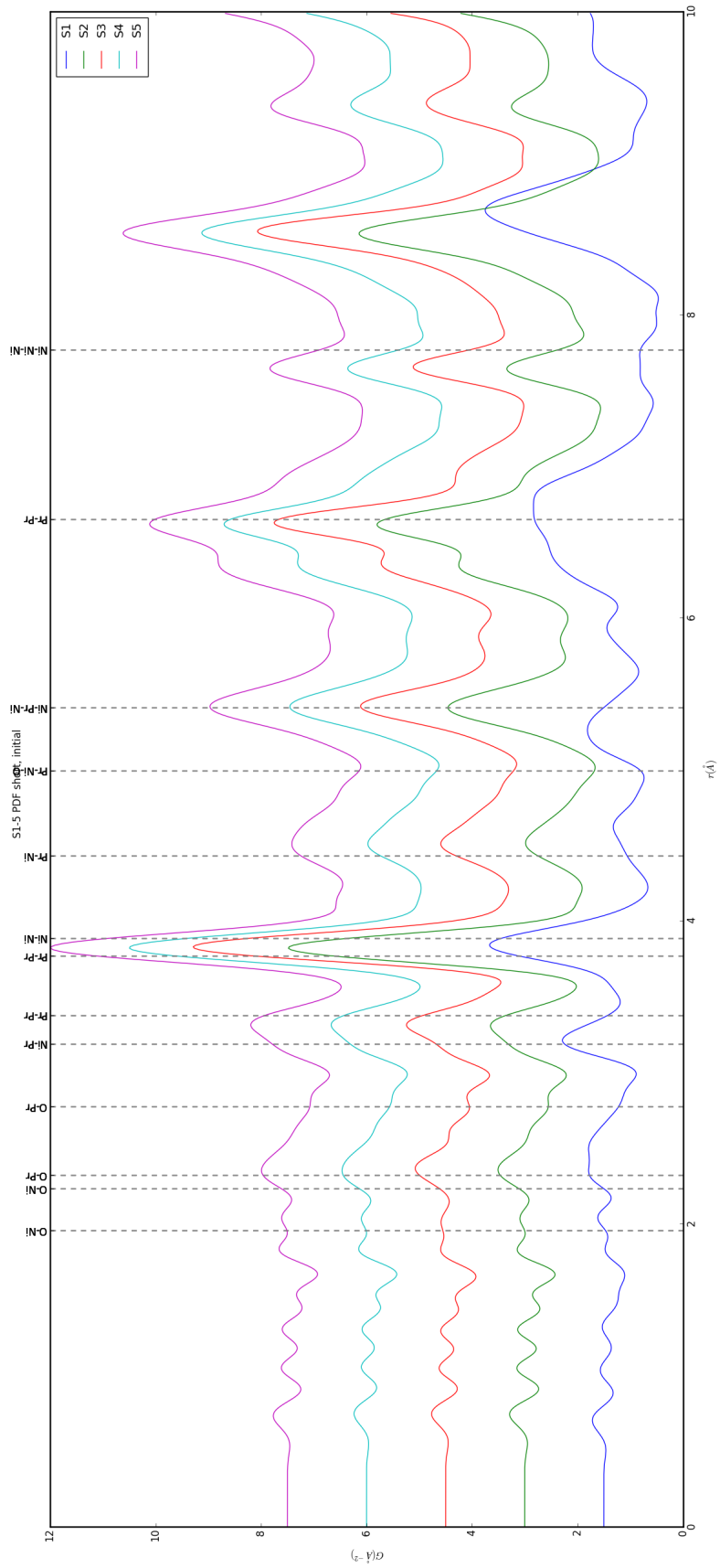


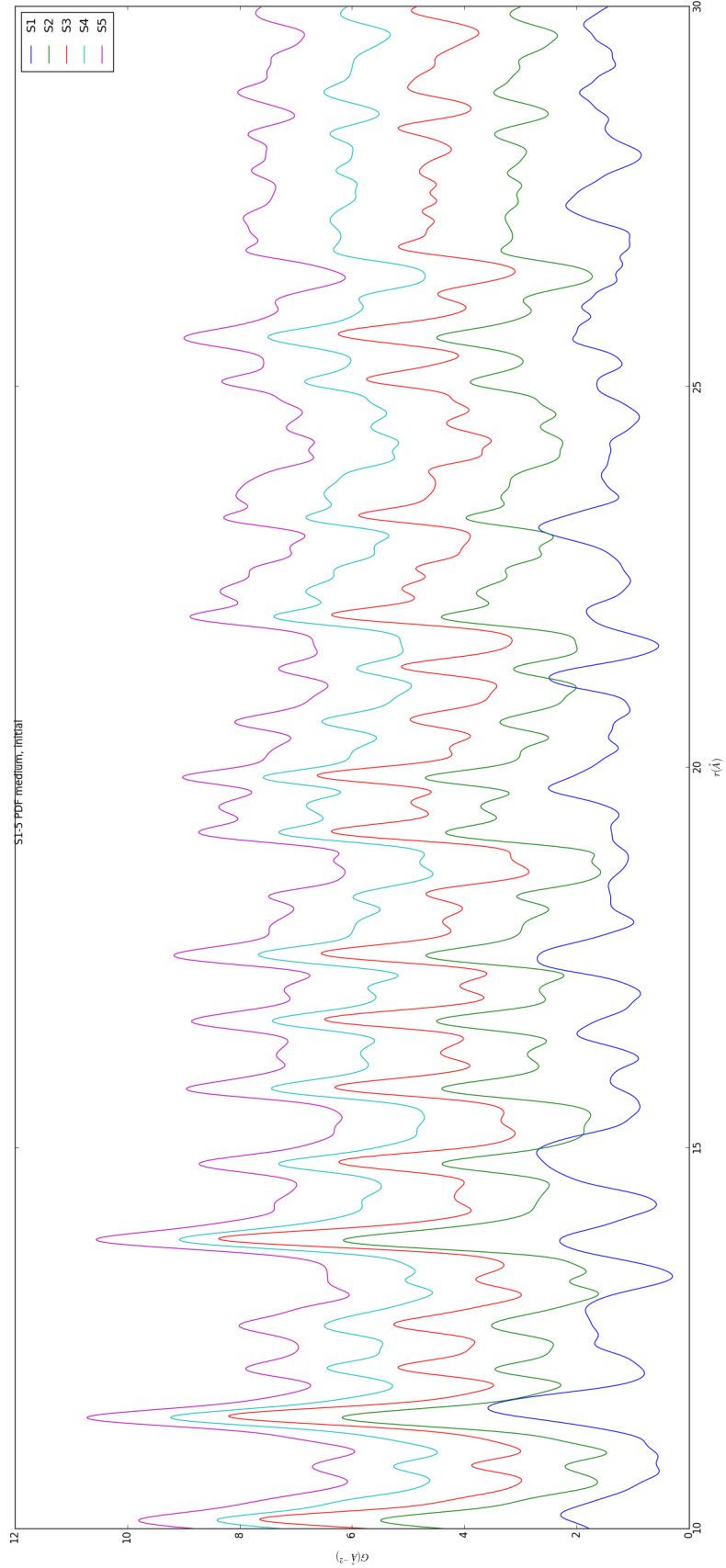
⁷⁴⁵ Inter Sample Comparison

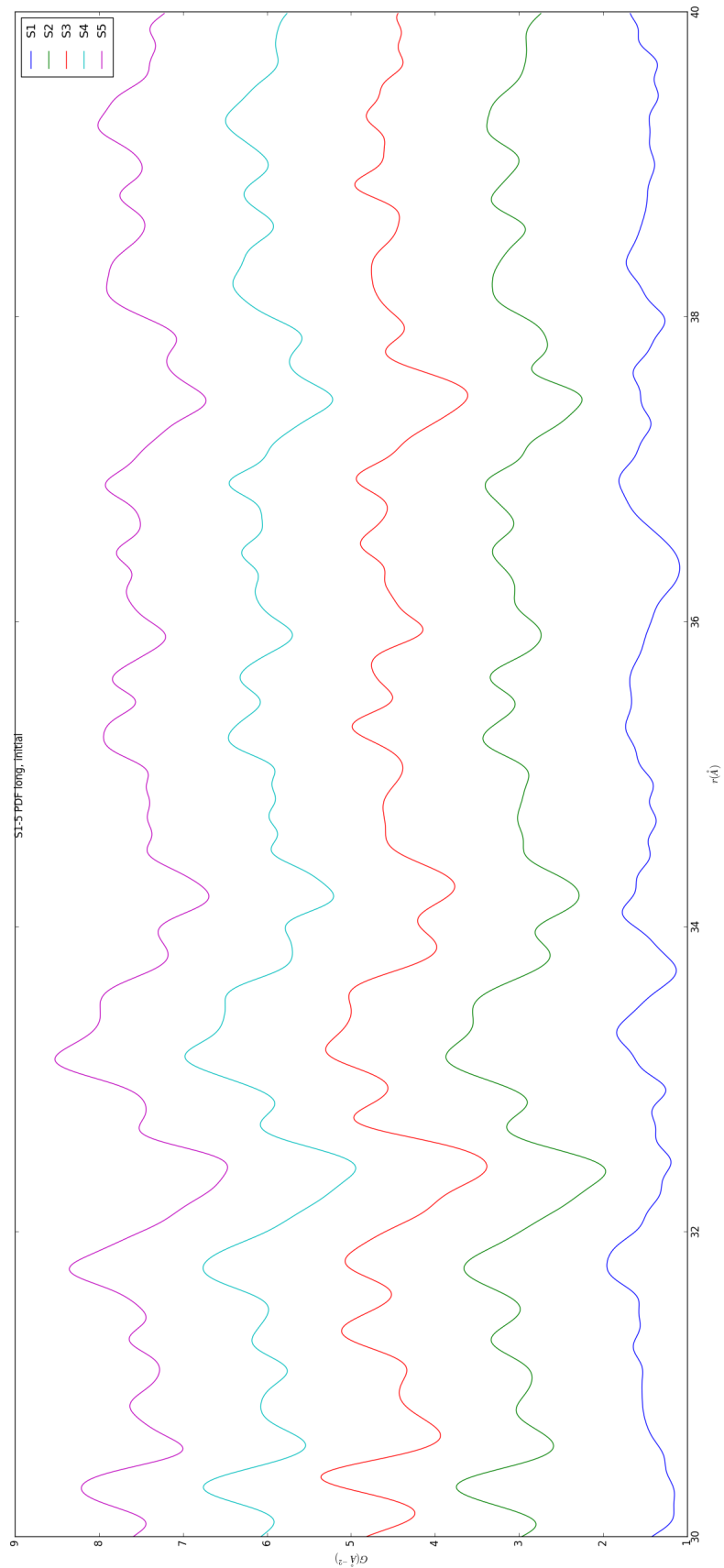


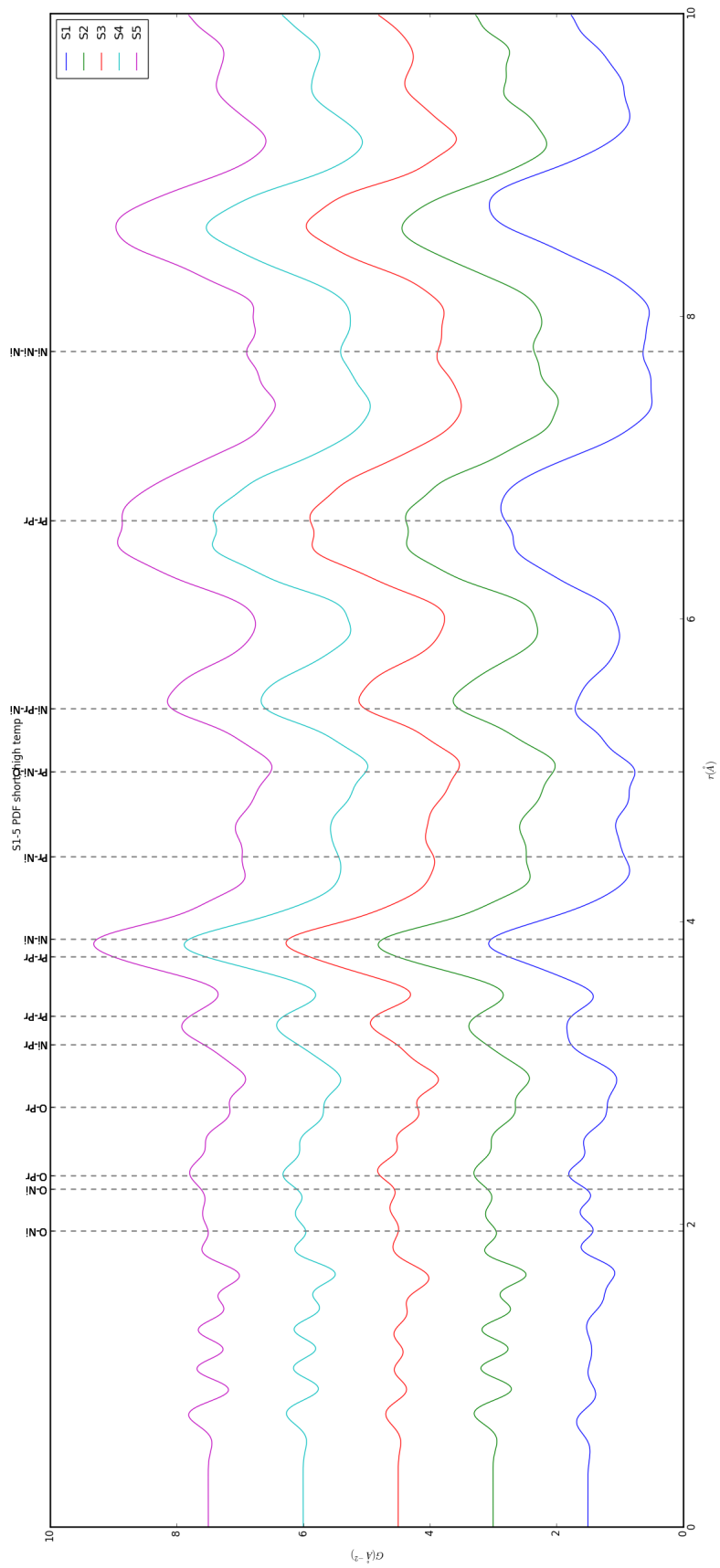


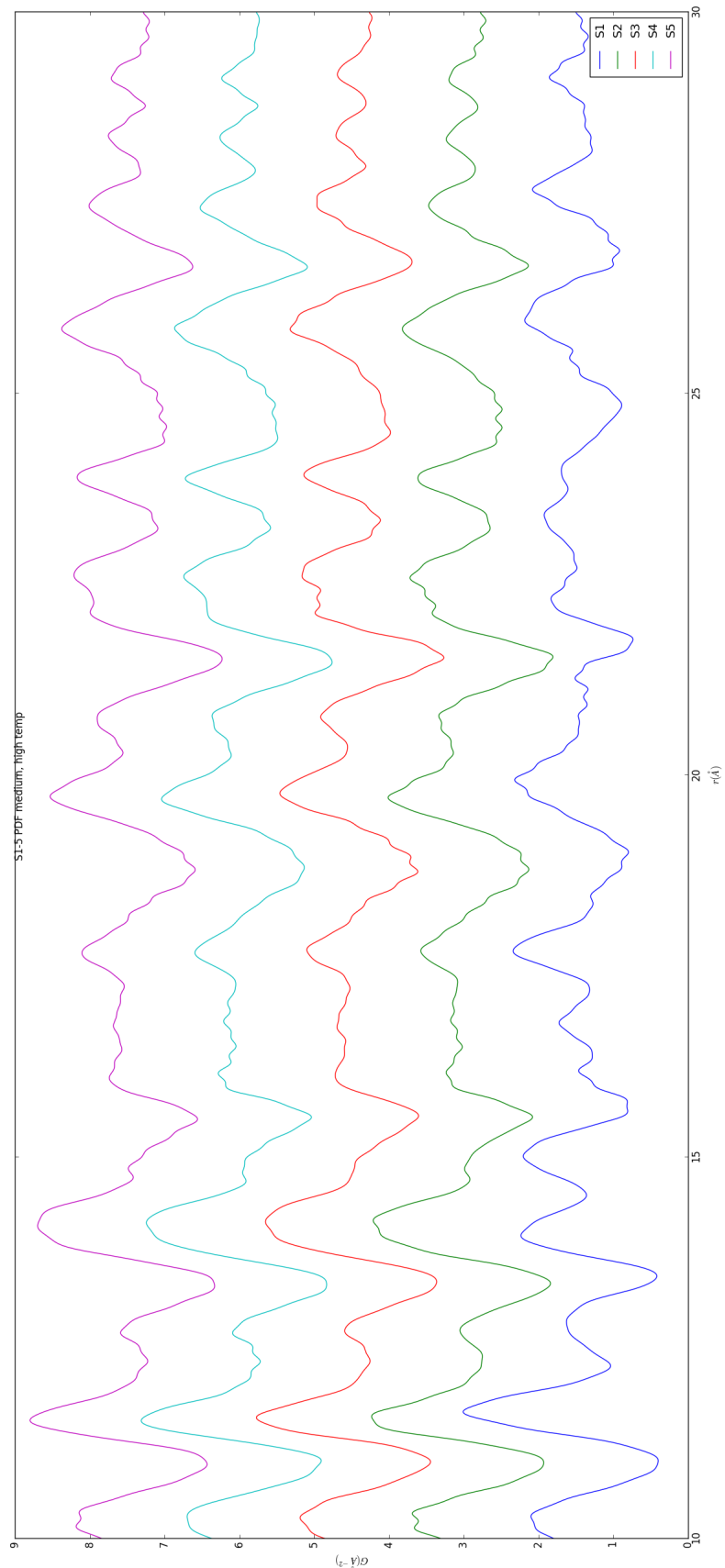


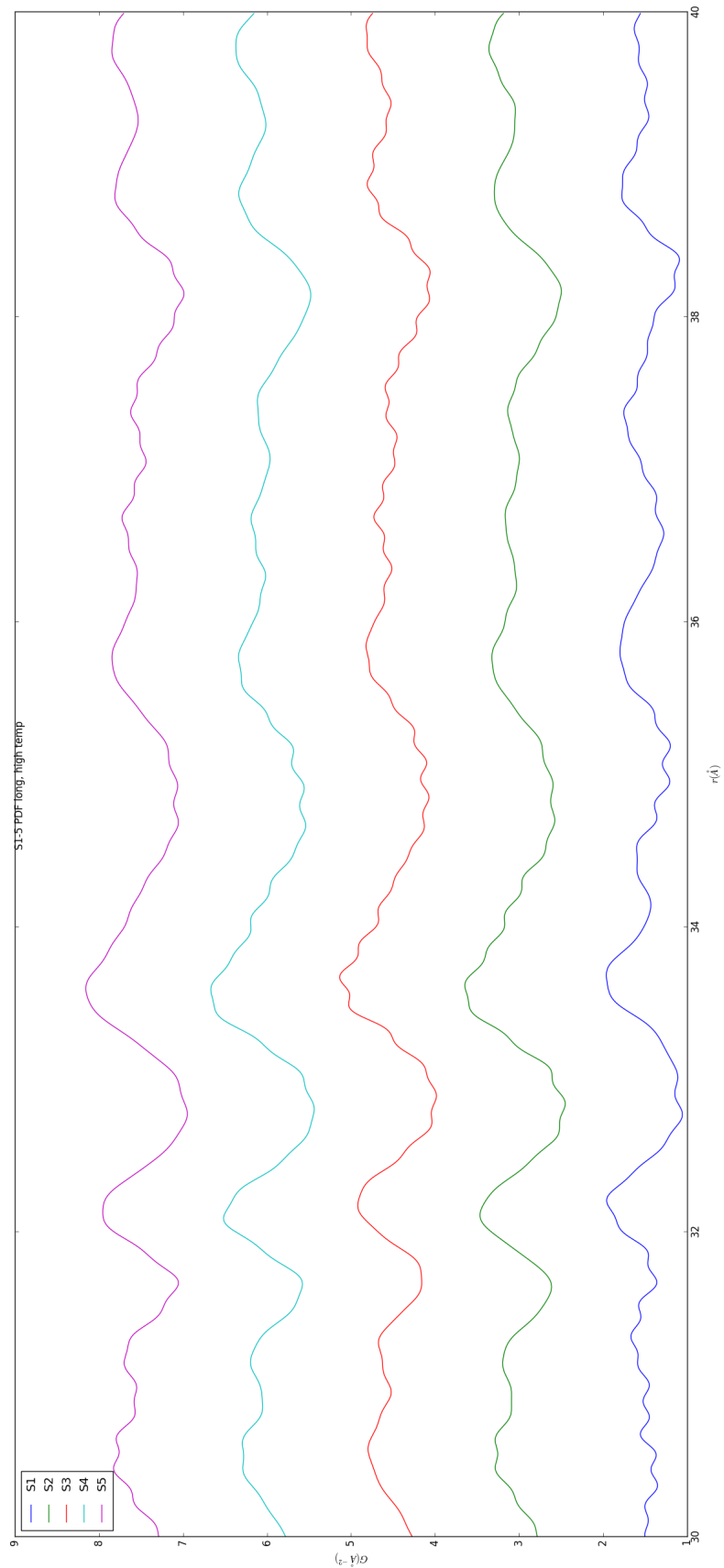


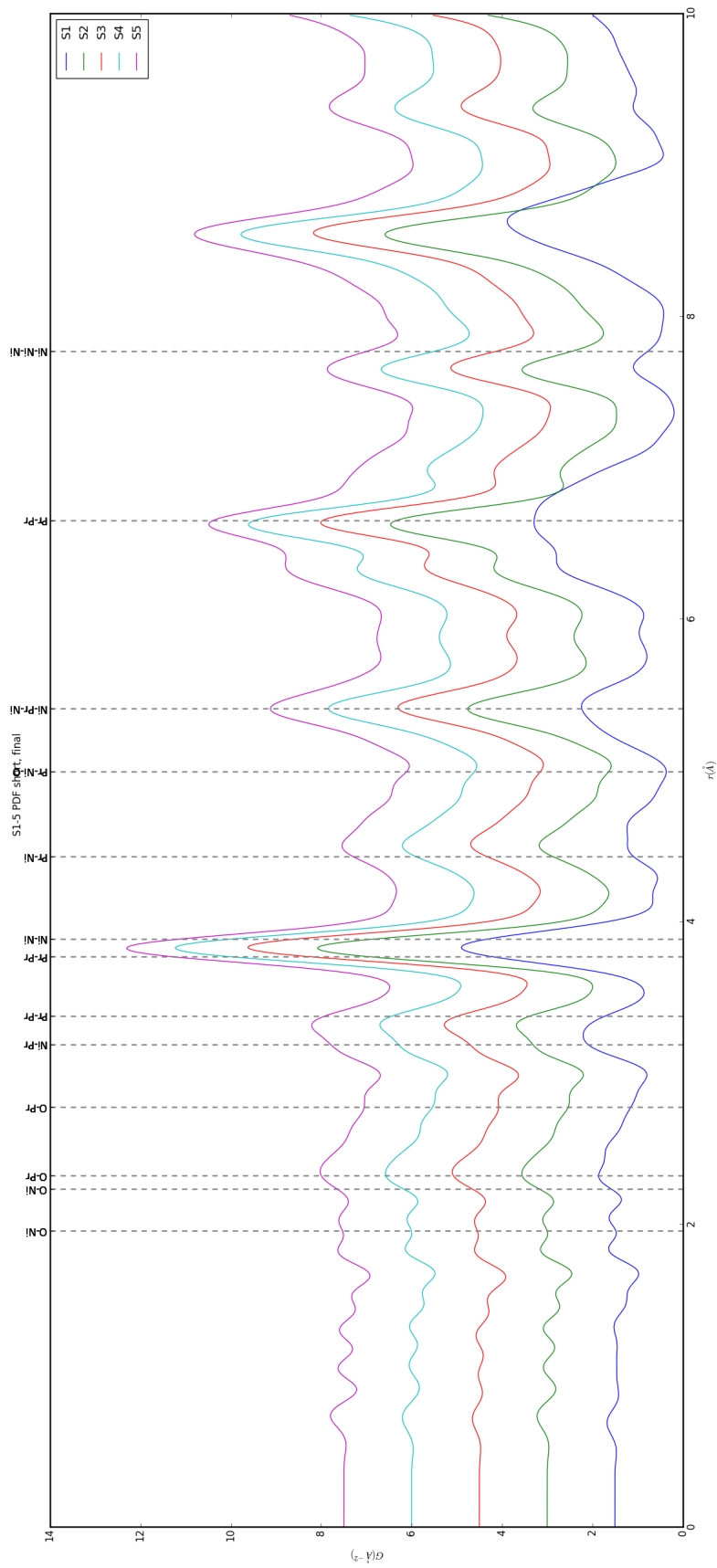


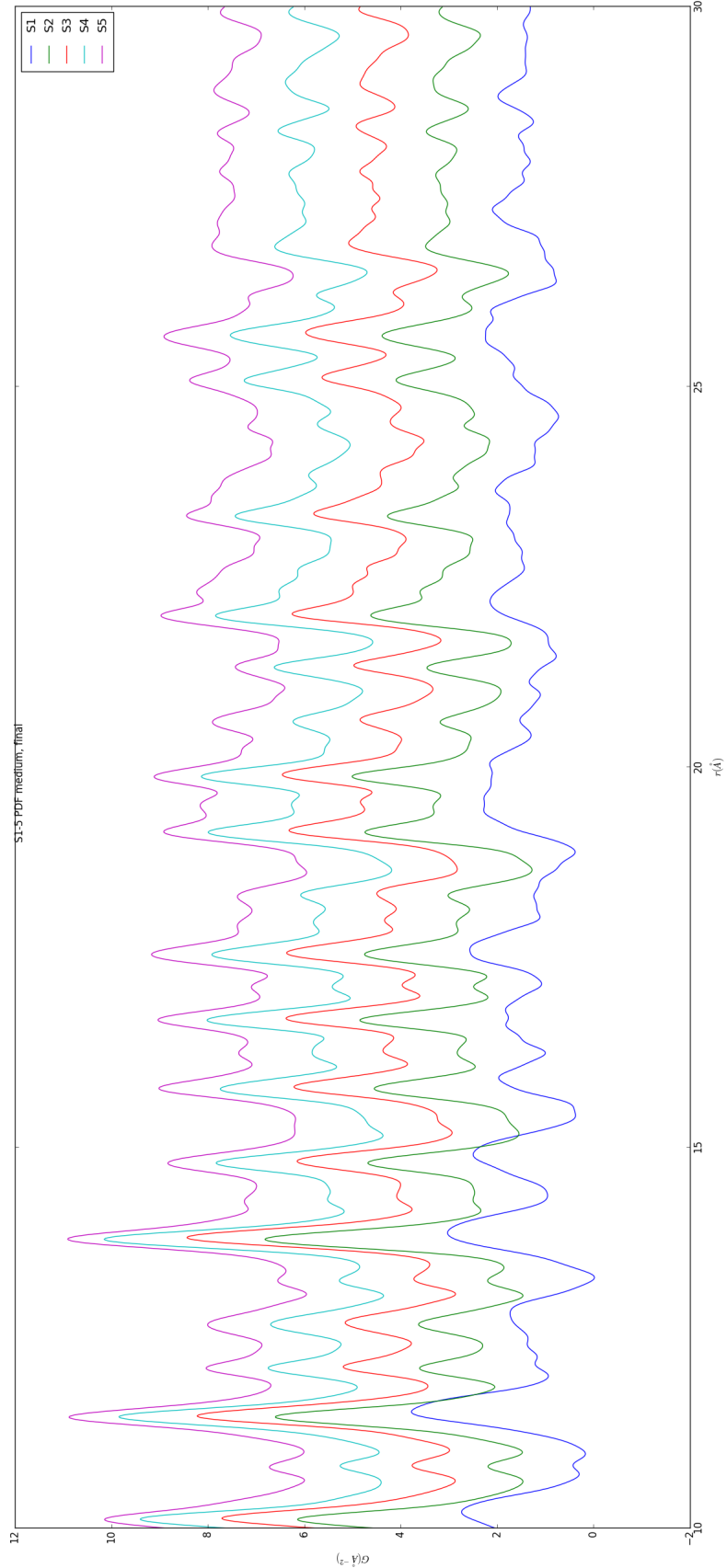


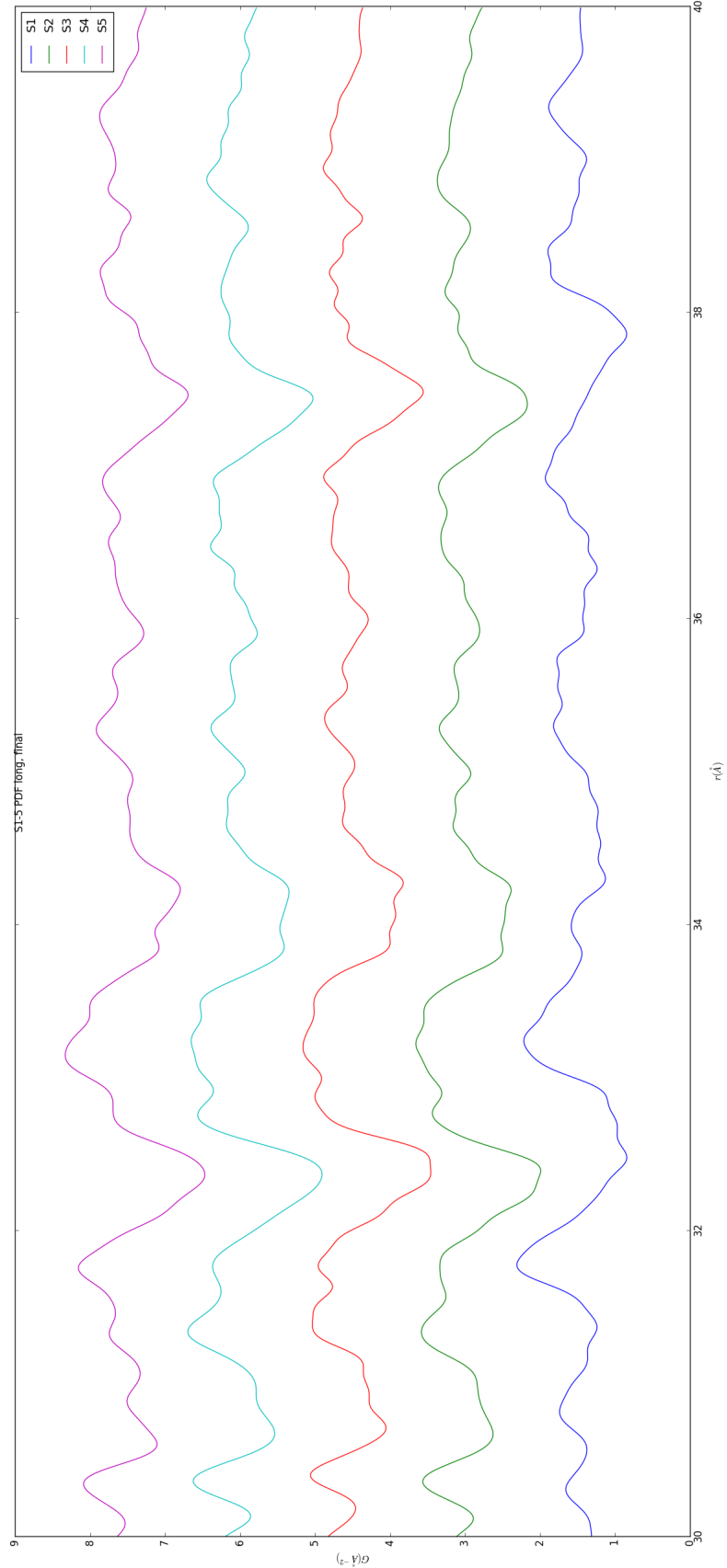












746 The PDF for S1 at operating temperature looks like S2-5 at the same temperature.

747 6.4 SIMULATION

748 Simulations have not been run yet on these PNO samples. Solving the structures of
749 these samples is expected to be more difficult than the NP benchmarks previously
750 solved. The difficulty of these simulations is due to:

- 751 1. The PDF's insensitivity to the oxygen positions, due to the poor x-ray scattering
752 off the very electorn poor oxygens.
- 753 2. The large difference in mass between the oxygen and other atoms, causing the
754 dynamics of the simulation to be governed by oxygen motion, nessecitating long
755 simulation times to obtain movement of the other atoms.
- 756 3. The large parameter space caused by potential defects and degradation prod-
757 ucts. Without knowing that the starting phase is pure, it is difficult to even
758 produce starting structures, since the simulation will need to explore all the
759 potential defect/degenerated structures.

760 6.5 CONCLUSIONS

761 X-ray total scattering and x-ray powder diffraction data was obtained on Pr_2NiO_4
762 powder samples annealed for various lengths of time. In-situ studies on the beamline
763 were performed to understand how the structure of each of these powders changes
764 at operating temperatures. The data was processed with the previously discussed Q
765 binning, masking, and integration methodology. The PDF results show very little
766 change in the structure for the as synthesized sample. However, the PDFs show a
767 large change in the previously annealed samples. These changes seem to reporduce
768 PDFs similar to the as-synthesized PNO at operating temperatures. This would seem
769 to imply that the source of the anamolus PNO phase/power density relationship may

770 be due to the adoption of an active structure upon heating which is universal despite
771 the amount of thermal degradation observed at room temperature. In contrast to the
772 PDF results, the XRD results seem to show signifigant changes in the PNO structure,
773 both with ex-situ and in-situ annealing. The XRDs show the degradation of the PNO
774 into various phases, potentially including Pr_2O_{11} , and higher ordered Pr based phases.
775 The discrepancy between these two results is quite interesting as it seems that the
776 XRD and PDF results are contradictory. Turbostratic diplacements between the
777 layers may be a cause of the PDF/XRD disagreement, as these changes would cause
778 very little change in the local structure observed in the PDF, while causing large
779 changes in the XRD.

780

CHAPTER 7

781

CONCLUSION

BIBLIOGRAPHY

- 783 [1] P. E. Blöchl, *Projector augmented-wave method*, Physical Review B **50** (1994),
784 no. 24, 17953–17979.
- 785 [2] Matthew J. Cliffe, Martin T. Dove, D. a. Drabold, and Andrew L. Goodwin,
786 *Structure determination of disordered materials from diffraction data*, Physical
787 Review Letters **104** (2010), no. 12, 1–4.
- 788 [3] Matthew J Cliffe and Andrew L Goodwin, *Nanostructure determination from the*
789 *pair distribution function: a parametric study of the INVERT approach.*, Journal
790 of physics. Condensed matter : an Institute of Physics journal **25** (2013), no. 45,
791 454218.
- 792 [4] Juarez L F Da Silva, Hyoung Gyu Kim, Maurício J. Piotrowski, Maurício J. Pri-
793 eto, and Germano Tremiliosi-Filho, *Reconstruction of core and surface nanopar-*
794 *ticles: The example of Pt 55 and Au55*, Physical Review B - Condensed Matter
795 and Materials Physics **82** (2010), no. 20, 1–6.
- 796 [5] C L Farrow, P Juhas, J W Liu, D Bryndin, E S Božin, J Bloch, Th Proffen, and
797 S J L Billinge, *PDFfit2 and PDFgui: computer programs for studying nanostruc-*
798 *ture in crystals.*, Journal of Physics. Condensed Matter : an Institute of Physics
799 journal **19** (2007), no. 33, 335219.
- 800 [6] Christopher L Farrow and Simon J L Billinge, *Relationship between the atomic*
801 *pair distribution function and small-angle scattering: implications for modeling*
802 *of nanoparticles.*, Acta Crystallographica Section A Foundations of Crystallog-
803 *raphy* **65** (2009), no. Pt 3, 232–9 (en).
- 804 [7] Riccardo Ferrando, Julius Jellinek, and Roy L Johnston, *Nanoalloys: From The-*
805 *ory to Applications of Alloy Clusters and Nanoparticles*, Chemical Reviews **108**
806 (2008), no. 3, 846–904.
- 807 [8] Pablo D Jadzinsky, Guillermo Calero, Christopher J Ackerson, David A Bushnell,
808 and Roger D Kornberg, *Structure of a thiol monolayer-protected gold nanoparti-*
809 *cle at 1.1 Å resolution.*, Science (New York, N.Y.) **318** (2007), no. 5849, 430–433.

- 810 [9] G. Kresse and J. Hafner, *Ab initio molecular dynamics for liquid metals*, Physical
811 Review B **47** (1993), no. 1, 558–561.
- 812 [10] ———, *Ab initio molecular-dynamics simulation of the liquid-
813 metalâŠamorphous-semiconductor transition in germanium*, Physical Review
814 B **49** (1994), no. 20, 14251–14269.
- 815 [11] Yan Li, Giulia Galli, and François Gygi, *Electronic structure of thiolate-covered
816 gold nanoparticles: Au102(MBA)44*, ACS Nano **2** (2008), no. 9, 1896–1902.
- 817 [12] L D Marks, *Experimental studies of small particle structures*, Reports on
818 Progress in Physics **57** (1994), no. 6, 603–649 (en).
- 819 [13] John P. Perdew, Kieron Burke, and Matthias Ernzerhof, *Generalized Gradient
820 Approximation Made Simple*, Physical Review Letters **77** (1996), no. 18, 3865–
821 3868.
- 822 [14] Andrew A. Peterson, *Global optimization of adsorbate-surface structures while
823 preserving molecular identity*, Topics in Catalysis **57** (2014), no. 1-4, 40–53.
- 824 [15] Valeri Petkov, Shiyao Shan, Peter Chupas, Jun Yin, Lefu Yang, Jin Luo, and
825 Chuan-Jian Zhong, *Noble-transition metal nanoparticle breathing in a reactive
826 gas atmosphere.*, Nanoscale **5** (2013), no. 16, 7379–87.
- 827 [16] H. W. Sheng, M. J. Kramer, A. Cadien, T. Fujita, and M. W. Chen, *Highly
828 optimized embedded-atom-method potentials for fourteen FCC metals*, Physical
829 Review B - Condensed Matter and Materials Physics **83** (2011), no. 13, 134118.